JOURNAL OF PROPULSION AND POWER
Vol. 27, No. 4, July–August 2011

Numerical Simulations of Liquid Rocket Coaxial Injector Hydrodynamics

John Tsohas* and Stephen D. Heister†
Purdue University, West Lafayette, Indiana 47906

DOI: 10.2514/1.47761

A series of unsteady Reynolds-averaged Navier–Stokes computations are made for a range of conditions pertinent to coaxial rocket injectors used on large liquid rocket engines with the intent of investigating unsteadiness resulting from hydrodynamic instabilities within the confines of the injector and in the near field of the injection point in the chamber. Axisymmetric simulations are conducted using a real fluid treatment for liquid oxygen and gaseous hydrogen propellants. An in-depth look inside the injector recess region was performed in an effort to characterize the dynamic character of mass flow pulsations created from hydrodynamic instabilities. Wake instabilities downstream of the liquid oxygen post tip, the acoustic pulsations within the liquid oxygen tube, and the vortex shedding from the injector lip all contribute to natural pulsations, even in the event of purely steady upstream and downstream conditions. The effects of varying the oxidizer/fuel ratio, the liquid oxygen post thickness, the liquid oxygen post length, and the liquid oxygen post acoustic frequency on injector frequency response were investigated.

Nomenclature

A = cell face area
D_s = species diffusion coefficient
e_0 = total energy of mixture
F_i = inviscid flux vector
F_v = viscous flux vector
NS = number of chemical species
$\tilde{n}$ = unit normal vector to a surface
p = pressure
Q = vector of conservative variables
$\tilde{q}$ = heat conduction vector
S_{ct} = Schmidt number
T = temperature
t = time
$\tilde{u}$ = velocity vector
$\tilde{V}_s$ = species mass diffusion velocity
$\dot{W}$ = chemistry source term vector
$\tilde{w}_s$ = species chemical production rate
Y_s = species mass fraction, ρ_s/ρ
$\partial\Omega_c$ = boundary of cell c
$\theta_{v,s}$ = species characteristic vibrational temperature
λ = coefficient of thermal conductivity
μ_t = coefficient of turbulent viscosity
ρ = density of mixture
ρ_s = species density
$\tilde{\tilde{\tau}}$ = stress tensor
Ω_c = control volume of cell c

I. Introduction

THE phenomenon of combustion instability has plagued the development of large liquid bipropellant rocket engines for many decades. In the early days of rocket engine development, and to some extent even today, combustion instability was corrected by extensive hot-fire testing of injector and chamber design variations until a suitable configuration was determined. However, rigorous hot-fire testing can be both expensive and time consuming. The advent of high-speed computing and computational fluid dynamics (CFD) has led to a better understanding of the inherent dynamics that contribute to the development of combustion instability in rocket thrust chambers. Increased modeling capabilities of internal flows can lead to better engine designs, thus contributing to a reduction in the number of costly hot-fire tests required to achieve stability.

Dynamic processes taking place inside the injector are major contributors to combustion instabilities exhibited in the thrust chamber. Pressure and propellant mass flow fluctuations from the injector may lead to droplet atomization and vaporization perturbations that can couple with the thrust chamber acoustic modes. Liquid oxygen (LOX) and gaseous hydrogen (GH_2) coaxial rocket injectors are currently used in the space shuttle main engine, RS-68, RL-10, and J-2 liquid rocket engines in the United States. This type of injector consists of an internal LOX post coaxially located inside a GH_2 tube, as shown in Fig. 1. LOX is injected into the combustion chamber through a central tube (LOX post) while hydrogen passes through the combustion chamber and nozzle cooling channels and is fed in gaseous form through an outside annular passage at a high velocity relative to the liquid jet. The large gas/liquid velocity ratios result in wave disturbances on the surface of the LOX jet, which lead to breakup and atomization by the formation of liquid ligaments and droplets. The resulting oxygen spray vaporizes and mixes with the gaseous fuel, creating a mixture suitable for combustion to take place. Hydrodynamic instabilities are present, even in the absence of upstream or downstream pressure oscillations in the injector, thus leading to self-pulsation or unforced injector response [1]. The high hydrogen gas velocities used in most designs makes the LOX surface highly unstable, and these instabilities can grow very rapidly, even within the submerged region upstream of the injector face. The characterization of these frequency and amplitude oscillations is important to prevent coupling with thrust chamber acoustic modes.

While the coaxial rocket injector enjoys a geometrical similarity with devices used in gas turbine engines, chemical separators/dryers, and food processing devices, the flow conditions in the rocket injector create the highest velocities, Reynolds numbers, and Weber numbers of any application of these devices. At more modest gas and liquid velocities, the Kelvin–Helmholtz (K–H) instability provides a length scale for mixing of the two streams; at rocket injection conditions, the K–H length scale is tiny, literally measured in microns. Prior liquid rocket injector studies have shown three major sources for hydrodynamic instability:

Received 22 October 2009; revision received 13 October 2010; accepted for publication 25 October 2010.

*Postdoctoral Researcher, School of Aeronautics and Astronautics, 701 West Stadium Avenue. Member AIAA.

†Professor, School of Aeronautics and Astronautics, 701 West Stadium Avenue. Associate Fellow AIAA.

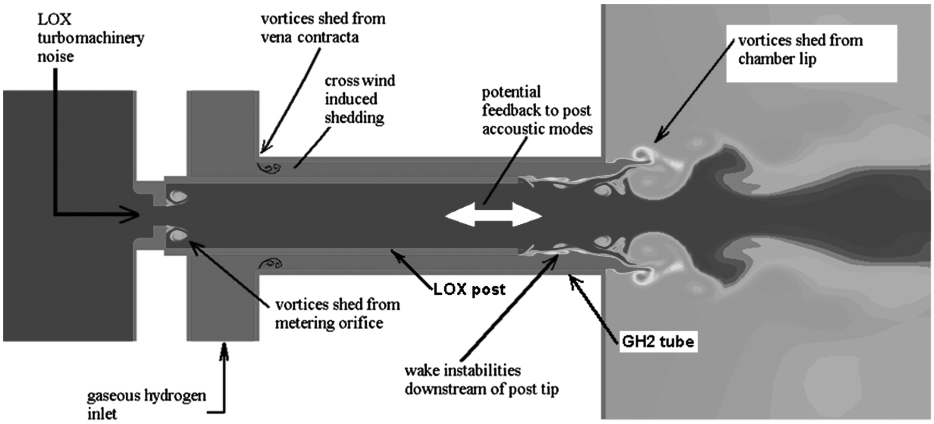

Fig. 1 Hydrodynamic processes of liquid rocket shear coaxial injector.

1) The first source is vortex shedding/wake instabilities of gaseous fuel and liquid oxidizer aft of the internal LOX post [1–3]. The very large dynamic pressures within the region just downstream of the post tip can create large three-dimensional (3-D) pulsations within the recessed region and into the near field as the mixture exits the element. The LOX post wake region (several LOX jet diameters downstream of the LOX post) controls the LOX/GH_2 mixing process, whereby the LOX/GH_2 propellants are separated by a layer of reacting combustion gases [4]. The thickness of the post tip is critically important, as it is generally acknowledged that this structure provides flame stabilization [5].

2) The second source is vortex shedding from the rearward-facing step created at the interface between the injector exit plane and the chamber faceplate, as shown in Fig. 1. While vortex shedding of plain jets is a well-studied field, the large disparity in fluid densities and velocities in the rocket application, combined with upstream vorticity shed from the LOX post tip, make this jet instability quite challenging to characterize.

3) The third source is acoustic pulsations within the LOX column residing within the LOX tube [6,7]. This source of pulsations has not received nearly as much study or mention in the literature, and there does not appear to be general agreement on the level of importance this instability may have.

High-frequency oscillations of the jet spray have been observed in experimental studies of coaxial injectors with a recessed LOX post. These disturbances couple with the dynamics of the jet breakup process and may provide amplification of the combustion chamber oscillations. Bazarov et al. have called this phenomenon self-oscillation, suggesting this is the cause of decreased combustion efficiency and a source of high-amplitude noise during combustion [8,9]. Combustion instabilities of this kind, in some cases, may lead to catastrophic failures [9].

There have been limited attempts to correlate hydrodynamic perturbations with combusting flows. Here, the principle difficulty is the potential resonance of the combustion process with chamber acoustic modes as well, so many more tones appear in combusting flows. Mayer and Tamura [4] had seen activity in the 6–7 kHz region in their single-element studies and, at about the same time, Kim and Heister [2,3] reported similar frequencies due to hydrodynamic instabilities within the recess cup. Additional evidence is coming available as comprehensive unsteady computations are within reach in the present computational environment. These factors provide strong motivation for the present study.

II. Computational Model

The Loci/CHEM code has been used to perform the computations discussed herein. For completeness, a brief discussion of the unstructured Navier–Stokes solver is discussed. The interested reader is referred to papers from Luke et al. for a detailed discussion of the numerics used in Loci/CHEM and rules-based computing [10–12].

A finite volume procedure is used to discretize the governing flow equations, which are presented in Eq. (1) in 3-D form with non-equilibrium chemistry and equilibrium internal energy:

$$\frac{\mathrm{d}}{\mathrm{d}t}\int_{\Omega_c(t)} Q\,\mathrm{d}V + \int_{\partial\Omega_c(t)} (F_i - F_v)\,\mathrm{d}S = \int_{\Omega_c(t)} \dot{W}\,\mathrm{d}V \tag{1}$$

where the vectors of conservative state variables Q, inviscid flux F_i, viscous flux F_v and the chemistry source term $\dot{W}$ are given by

$$Q = \begin{bmatrix} \rho_1 \\ \vdots \\ \rho_s \\ \vdots \\ \rho_{\mathrm{NS}} \\ \rho\tilde{u} \\ \rho e_0 \end{bmatrix} \qquad F_i = \begin{bmatrix} \rho_1 \tilde{u}\cdot\tilde{n} \\ \vdots \\ \rho_s \tilde{u}\cdot\tilde{n} \\ \vdots \\ \rho_{\mathrm{NS}} \tilde{u}\cdot\tilde{n} \\ (\rho\tilde{u}\,\tilde{u} + p\tilde{\tilde{I}})\cdot\tilde{n} \\ (\rho e_0 + p)\tilde{u}\cdot\tilde{n} \end{bmatrix}$$

$$F_v = \begin{bmatrix} \rho_1 \tilde{V}_1\cdot\tilde{n} \\ \vdots \\ \rho_s \tilde{V}_s\cdot\tilde{n} \\ \vdots \\ \rho_{\mathrm{NS}} \tilde{V}_{NS}\cdot\tilde{n} \\ \tilde{\tilde{\tau}}\cdot\tilde{n} \\ (\tilde{u}\cdot\tilde{\tilde{\tau}} + \tilde{q} + \sum \rho_s h_s \tilde{V}_s)\cdot\tilde{n} \end{bmatrix} \qquad W = \begin{bmatrix} \dot{w}_1 \\ \vdots \\ \dot{w}_s \\ \vdots \\ \dot{w}_{\mathrm{NS}} \\ 0 \\ 0 \end{bmatrix} \tag{2}$$

In the present study, the pressure term is determined from either using Dalton's law for the ideal gas cases or the CHEM real fluids model for the real fluids cases. Dalton's law simply states that the pressure of the mixture of gases is equal to the sum of partial pressures of each individual species, and each species behaves as a thermally perfect gas.

In Eq. (3), pressure is related to gas temperature, which is determined from the internal energy e_{int}:

$$\begin{aligned} e_0 &= e_{\mathrm{int}} + \text{kinetic} + \text{chemical} + \text{latent} \\ &= \sum_i^{\mathrm{NS}} Y_i(e_{\mathrm{int}}) + \frac{u^2}{2} + \sum_i^{\mathrm{NS}} Y_i(e_{f,i}) + \sum_i^{\mathrm{NS}} Y_i(e_{L,i}) \end{aligned} \tag{3}$$

For a mixture of fluids, the thermal energy contributions may be written as follows:

$$e_{\mathrm{int}} = \int_{T_r}^{T} c_{v,i}\,\mathrm{d}\tau + \mathrm{correction}_i \tag{4}$$

For mixtures of thermally perfect gases, the correction term is equal to zero. For mixtures of fluids, these terms are rather involved (see Cinnella et al. [13]).

To close the system of equations, the stress tensor, the heat flux vector, and the species diffusion velocities that appear in the viscous flux must be defined. Only Newtonian fluids are considered here. Moreover, Fourier's law is employed to relate heat conduction and temperature gradients. Under these assumptions, the stress tensor and heat flux vector in tensor notation can be written as

$$\tau_{i,j} = (\mu + \mu_t)\left(\frac{\partial u_i}{\partial x_j} + \frac{\partial u_j}{\partial x_j}\right) - \frac{2}{3}[(\mu + \mu_t)\nabla \cdot u]\delta_{ij} \qquad (5)$$

$$\tilde{q} = (\lambda + \mu_t c_p / Pr_t)\nabla T \qquad (6)$$

A constant Prandtl number, $Pr_t = 0.9$, is used in all computations.

The transport properties of the mixture (namely, viscosity coefficient μ and thermal conductivity λ) are usually evaluated in two steps. First, the transport property of each species is determined, and then the mixture rule is applied in order to obtain mixture values. Two models are used to compute species transport properties. At temperatures lower than 1000 K, Sutherland's model is used, as shown in Eq. (7):

$$t_i = T^{3/2}\frac{F_{t,i}}{T + G_{t,i}} \qquad (7)$$

where t_i stands for either μ_i or λ_i, and $F_{t,i}$ and $G_{t,i}$ are constants determined empirically. For temperatures higher than 1000 K, a more accurate model based on curve fit tabulation proposed by Gupta et al. is used [14]:

$$\mu_i = \exp(C_{\mu,i})T^{A_{\mu,i}\,\ell n\,T + B_{\mu,i}} \qquad (8)$$

$$\lambda_i = \exp(E_{f,i})T^{[A_{f,i}(\ell n\,T)^3 + B_{f,i}(\ell n\,T)^2 + C_{f,i}\,\ell n\,T + D_{f,i}]} \qquad (9)$$

$A_{\mu,i}$, $B_{\mu,i}$, $C_{\mu,i}$, $A_{f,i}$, $B_{f,i}$, $C_{f,i}$, $D_{f,i}$, and $E_{f,i}$ are tabulated curve fit coefficients.

Once the individual species transport properties are obtained, the mixture transport properties are determined using Eq. (10):

$$t = \sum_{i=1}^{\mathrm{NS}} W_i t_i \qquad (10)$$

where t denotes the transport properties for the mixture (μ or λ), and the weighting function W_i is given by

$$W_i = \frac{X_i}{\sum_{j=1}^{\mathrm{NS}} X_j \Phi_{ij}} \qquad (11)$$

where the coefficient Φ_{ij} is given by

$$\Phi_{ij} = \frac{1}{\sqrt{8}}\left(1 + \frac{M_i}{M_j}\right)^{-1/2}\left[1 + \sqrt{\frac{\mu_i}{\mu_j}}\left(\frac{M_i}{M_j}\right)^{1/4}\right]^2 \qquad (12)$$

The species diffusion velocity $\tilde{V}_s$ is modeled using Fick's law of diffusion as

$$\rho_s \tilde{V}_s = -\left(\rho D_s + \frac{\mu_t}{Sc_t}\right)\nabla Y_s \qquad (13)$$

where D_s is the diffusion coefficient, μ_t is the eddy viscosity, and Sc_t is the turbulent Schmidt number (equal to 0.9).

The species diffusion coefficient D_s can be obtained by user specification or the CHEMKIN transport library. The current study defined a constant diffusion coefficient for each component based on fluid viscosity and a laminar Schmidt number of 0.9. Furthermore, all computations used the Menter shear stress transport (SST) model for computation of the turbulent kinetic energy and dissipation rate [15].

The numerical scheme used in CHEM is a finite volume scheme that supports generalized grids composed of arbitrary polyhedra, tetrahedral, prisms, pyramids, and hexahedra. The numerical integration of Eq. (1) begins with approximations to volume and surface integrals. For the volume integrals, a second-order midpoint rule is used. For instance, the numerical integration of Q results in

$$\int_{\Omega_C(t)} Q(\tilde{x}, t)\,\mathrm{d}V = Q_c(t)V_c(t) \qquad (14)$$

where $Q_c(t)$ is the value of Q at the centroid of cell c, and $V_c(t)$ is defined by

$$V_c(t) = \int_{\Omega_C(t)} \mathrm{d}V \qquad (15)$$

The numerical integration of the surface integral in Eq. (1) is accomplished by summing the contributions of each of the number of faces of cell c. Each individual contribution is again approximated using the midpoint rule. The flux function itself will require additional numerical treatment, and it will be discussed in later sections. For now, assume that the flux can be approximated by a function F of conservative value to the left and right of the face. Given this, the numerical integration of $F = F_i - F_v$ results in the following:

$$\int_{\vartheta\Omega_c(t)} F\,\mathrm{d}S = \sum_{f=1}^{\mathrm{NF}_c}\int_{\vartheta\Omega_{c,f(t)}} F\,\mathrm{d}S \approx \sum_{f=1}^{\mathrm{NF}_c} A_{c,f}(t)\hat{F}_f \qquad (16)$$

where the area of the face $A_{c,f}(t)$ is defined as

$$A_{c,f}(t) = \int_{\Omega_c(t)} \mathrm{d}S \qquad (17)$$

At this point, Eq. (1) is numerically approximated by the equation

$$\frac{\mathrm{d}}{\mathrm{d}t}[V_c(t)Q_c(t)] + \sum_{f=1}^{\mathrm{NF}} A_{c,f}(t)\hat{F}_f = V_c(t)\dot{W}_c(t) \qquad (18)$$

The differential term that remains in this equation applies to the product of the volume and the conservative state vector for the cell. However, the variable that is the objective of these calculations is $Q_c(t)$ and not $V_c(t)\ Q_c(t)$. This problem is solved by applying the chain rule:

$$\frac{\mathrm{d}}{\mathrm{d}t}Q_c(t)V_c(t) = Q_c(t)\frac{\mathrm{d}}{\mathrm{d}t}V_c(t) + V_c(t)\frac{\mathrm{d}}{\mathrm{d}t}Q_c(t) \qquad (19)$$

The derivative of the volume with respect to time can be converted into a spatial integral through the use of an identity for integration over time-dependent domains:

$$Q_c\frac{\mathrm{d}}{\mathrm{d}t}V_c(t) = Q_c\frac{\mathrm{d}}{\mathrm{d}t}\int_{\Omega_c}\mathrm{d}V = Q_c\int_{\vartheta\Omega_c(t)}\tilde{u}_\Omega \cdot \tilde{n}\,\mathrm{d}S \approx Q_c\sum_{f=1}^{\mathrm{NF}_c} A_{c,f}(t)(\tilde{u}_{\Omega,f} \cdot \tilde{u}_{c,f}) \qquad (20)$$

This equation, known as the geometric conservation law, is necessary for correct time integration when mesh deformation is present. Given this, the solution method can now be described in terms of a system of ordinary differential equations of the form

$$V_c\frac{\mathrm{d}}{\mathrm{d}t}Q_c = R_c \qquad (21)$$

where R_c is given by the expression

$$R_c = V_c\Delta_c\dot{W}_c - \sum_{f=1}^{\mathrm{NF}_c} A_{c,f}\hat{F}_f - Q_c\sum_{f=1}^{\mathrm{NF}_c} A_{c,f}(\tilde{u}_{\Omega,f} \cdot \tilde{n}_{c,f}) \qquad (22)$$

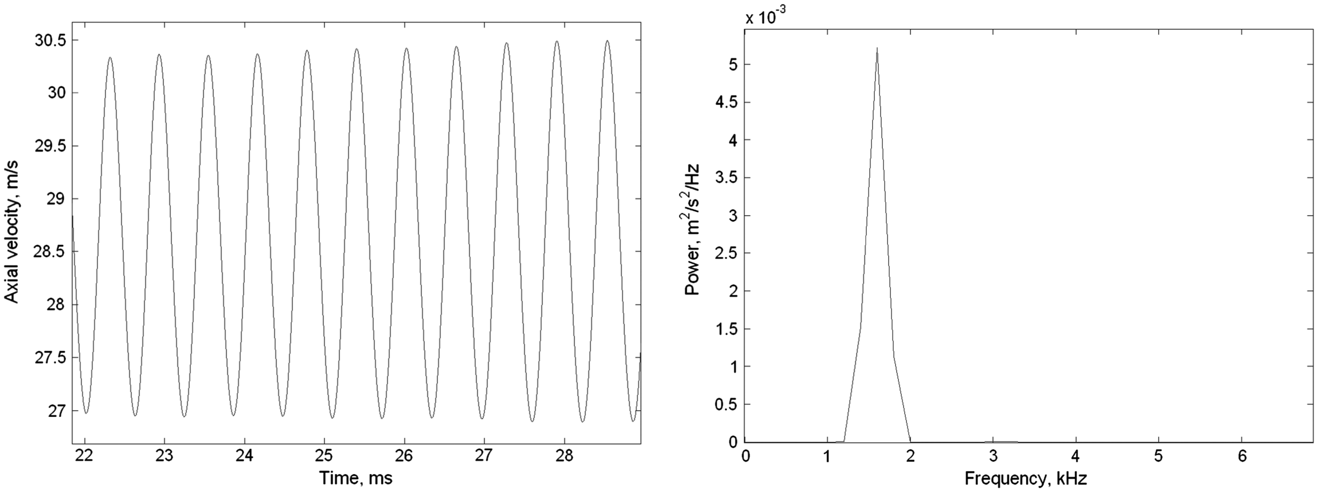

Fig. 2 Axial velocity (left) and PSD plot (right) at probe point of Eisenlohr and Eckelmann [19] experiment computation.

Equations (21) and (22) describe a system of ordinary differential equations that numerically model the time evolution of the fluid dynamics equations when simultaneously satisfied for all cells in the mesh. To represent this fact, the cell subscript c will be dropped. Thus, Q_c represents the fluid state for cell c, while Q represents the fluid states of all cells in the mesh. For example, while Eq. (20) represents the cell-by-cell differential equations, the global system of equations in given by

$$V\frac{\mathrm{d}}{\mathrm{d}t}Q(t) = R(Q(t), t) \tag{23}$$

The inviscid terms of the Navier–Stokes equations are treated using standard flux-difference-splitting techniques. To evaluate the viscous fluxes, mixture density and velocity at each face are needed, as well as gradients of species mass fractions, velocities, and temperatures. Face values are evaluated by using a simple volume-weighted average of the integrated cell values on either side of the face. To compute face gradients, the first step is to determine the average of the least-squares gradient computed for the cells on either side of the face using the procedure for inviscid fluxes. The second step is to compute the gradient in the direction normal to the face. Finally, the previous two gradients are combined, as shown in Eq. (24):

$$\nabla\Phi_f = \nabla\Phi_{\mathrm{avg}} - (\nabla\Phi_{\mathrm{avg}}\cdot\tilde{n})\tilde{n} + \frac{\Phi(\tilde{x}_{c,c}) - \Phi(\tilde{x}_{d,c})}{(\tilde{x}_{c,c} - \tilde{x}_{d,c})\cdot\tilde{n}}\tilde{n} \tag{24}$$

where Φ is the quantity under consideration. Furthermore, the threshold limiter proposed by Venkatakrishna is used in the flux calculations [16]. The thresholding is designed to allow small overshoots in relatively smooth regions while strongly enforcing limiting where strong perturbations are present. For more details on the Venkatakrishnan limiter, please refer to [16]. The implicit time integration scheme employs a two-parameter family of algorithms, as shown in Eq. (25):

$$\begin{aligned} V[(1+\Psi)\Delta Q^n - \Psi\Delta Q^{n-1}] \\ = \Delta t\{(1-\theta)R^n(Q^n) + \theta R^{n+1}(Q^{n+1})\} \end{aligned} \tag{25}$$

where n is the current time step and $\Delta Q^n = Q^{n+1} - Q^n$. Parameters θ and ψ are two parameters that determine the accuracy of the time-integrated algorithms. For example, setting $\theta = 1$ and $\psi = 0$ gives the implicit backward Euler scheme typically used in steady-state simulations, while the second-order three-point backward scheme ($\theta = 1$ and $\psi = \frac{1}{2}$) is used for time-accurate simulations. Finally, to solve the discrete equations, nonlinear iterations are performed using Newton's method, while linear inner iterations are performed using Gauss–Seidel iterations for the ideal gas simulations or the PetSC solver for the real fluid cases.

III. Validation of Loci/CHEM Code

The performance of the Loci/CHEM code in replicating hydrodynamic instabilities and unsteadiness is of great interest to the present study. For this reason, a series of validation studies were performed to assess its performance with respect to well-documented benchmark cases.

To validate the Loci/CHEM code for low-speed flow, a test case was performed using data from the NASA John H. Glenn Research Center at Lewis Field, National Program for Applications-Oriented Research in CFD Alliance CFD Verification and Validation Archive.[‡] This validation case is called laminar flow over a circular cylinder, and it involves incoming flow over a two-dimensional (2-D) cylinder at a Reynolds number of 150 based on cylinder diameter. For this case, the incoming freestream Mach number is 0.2 at an ambient pressure of 0.00045146 psia and a temperature of 500°R. At this Reynolds number, the flow is laminar and produces 2-D vortical structures that are shed downstream of the cylinder in a periodic fashion. The dimensionless shedding frequency or Strouhal number and the average drag coefficient are compared with the experimental results from Roshko [17]. The experimental value of the Strouhal number for $Re = 150$ ranges from 0.179–0.182 [17], and the computed Strouhal number for all simulations was equal to 0.180–0.182, which lies well within the experimental range. For more details on this validation study, please refer to [18].

The next series of validation runs aims to exercise the Loci/CHEM code in solving problems that are more representative of the shear coaxial injector configuration. For this reason, the code is used to simulate the thin flat-plate experiment performed by Eisenlohr and Eckelmann [19]. In this experiment, the two unstable shear layers that shed behind the blunt trailing edge of a thin flat plate create vortices and promote the development of a vortex street that travels downstream. The results from the simulations show periodic vortex shedding from the backward-facing step of the flat plate, and a clean sinusoidal function is created with a single peak in the power spectral density (PSD) plot, as shown in Figs. 2 and 3, respectively. The PSD plots were generated using the spectrogram function in MATLAB. A total of 1500 time steps ($1e$-7 s per time step) were used to create each of the PSD plots, with an accompanying signal resolution of 67 Hz.

The calculated Strouhal number from the turbulent numerical simulations was equal to 0.26, which lies in line with the experimental data at the Reynolds number of 10,300. Again, further details on this particular validation study can be found in [18].

Thus far, the preceding validation runs were used to test the Loci/CHEM code under low-speed conditions and with two streams of air in a shear coaxial injector configuration. This was primarily a test of

---

[‡] Data available at http://www.grc.nasa.gov/WWW/wind/valid/ [retrieved 2011].

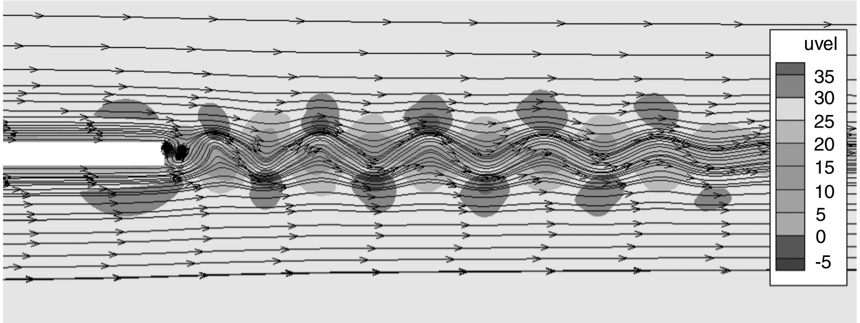

Fig. 3 Streamlines and axial velocity contour plots for Eisenlohr and Eckelmann [19] experiment.

the ideal gas model for air. The real fluids model was tested once during the LOX flow over a cylinder case described previously, and a third test case was performed to test the real fluids model in a shear coaxial injector configuration and to compare with experimental results. For this purpose, the DLR, German Aerospace Center (DLR) LOX/methane, shear coaxial injector experiment provides an excellent opportunity for comparison with its experimental data [6]. In this experiment, a series of single shear coaxial injectors were used to inject LOX and methane at pressures between 588 and 882 psia (40 to 60 atm), covering subcritical, near-critical, and supercritical pressures with respect to the critical point for oxygen (731 psia). We are interested in the case that operates at supercritical conditions in order to make use of the Loci/CHEM real fluids model for LOX. The engine was operated at an average oxidizer/fuel (O/F) ratio of 3.4, an F/O momentum ratio of 6.9, with LOX and methane injection velocities of 12.3 and 150.2 m/s, respectively. The LOX and gaseous methane were injected at temperatures of 120 and 283 K, respectively [6]. Note that the O/F mixture ratio was kept constant for all the tests. A detailed view of the recessed shear coaxial injector element is depicted in Fig. 4.

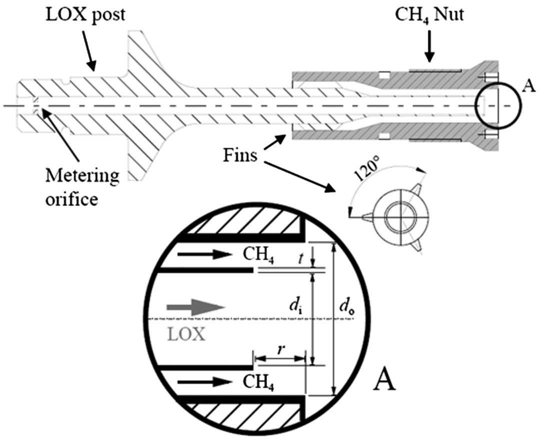

Fig. 4 Shear coaxial injector element with recessed LOX post. Image from Lux and Haidn paper [6].

Six different shear coaxial injector configurations were tested. All tests were performed using a LOX post with an inner diameter d_i equal to 5.6 mm and a wall thickness of 0.3 mm. Three configurations included no recess region, while the other three had a recess length r equal to 0.67 times the inner diameter of the LOX post d_i. The tested outer annulus diameter d_o was equal to 7.0, 7.2, and 7.4 mm. The computational domain has a chamber length equal to 143.3 mm (corresponding to one-third of the length of the actual chamber) and an inner diameter of 50 mm. To establish a velocity profile, the computational domain for the length of the LOX post was set to 24 mm, which corresponds to 4.3 LOX post diameters. Finally, this computational domain contains a total of 46,000 grid points.

To compare most effectively with experimental data, integrated mass flow rate data were obtained by probing across 10 distinct vertical planes inside the computational domain. These axial stations were located at the inlet plane, the manifold feed lines, the recess region, and the chamber domain. Since most dynamic activity takes place inside the narrow LOX post recess region of the injector, 10 axial locations (x-stations) were placed inside the injector recess region, as shown in Fig. 5. X-stations 1, 2, and 3 R are located inside the feed line region just before the LOX post tip. X-station 4 R is located exactly at the LOX post tip, the place where the upper and lower streams first make contact with each other. X-stations 5, 6, and 7 R are located inside the recess region, while x-station 8 R is located

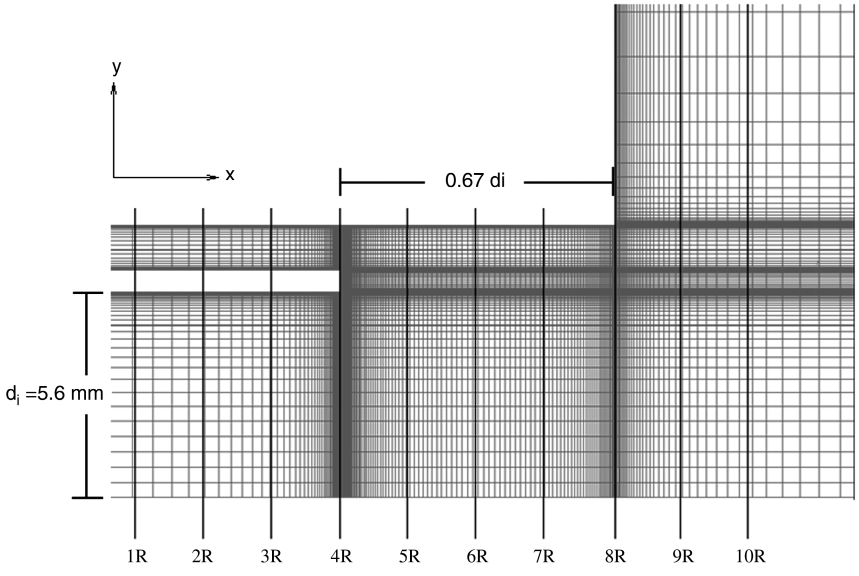

Fig. 5 Injector recess region x-station locations.

Table 1 Longitudinal modes of combustion chamber ($Lcc = 430$ mm) [6]

Mode	j	$f_{\text{theoretical}}$	f_{measured}	Deviation, %
1 L	1	1907	1820	−4.78
2 L	2	3814	3810	−0.10
3 L	3	5721	5670	−0.90
4 L	4	7628	7490	−1.84
5 L	5	9535	9270	−2.86

exactly at the injector exit plane (chamber faceplate). X-stations 9 and 10 R are located just inside the chamber region. In addition, pointwise probing inside the domain was performed to obtain velocity, pressure, and density values at each time step. These nine distinct probe points were located inside the manifold feed lines, the recess region, and the chamber domain, with extra points added at the post tip and injector exit plane to capture the behavior of the flow in this highly dynamic region.

Because of the large length-to-diameter ratio of the chamber, the theoretical frequencies can be calculated by using Eq. (26).

$$f_{\text{theoretical}} = \frac{j \cdot \bar{a}}{2 \cdot L} \tag{26}$$

where $j = 1, 2, 3, \ldots, \bar{a}$ is the mean speed of sound, and L is the length of the chamber. The theoretical and measured natural frequencies for this experiment are presented in Table 1.

For the validation simulations, we chose to model the recessed injector case ($r = 0.67 d_i$) with an outer annulus dimension d_o equal to 7.4 mm at supercritical injection pressures. Figure 6 depicts the PSD plot from the chamber pressure measurements. From the PSD data, it is evident that the first four peaks correspond closely to the theoretical natural frequencies (1 to 4 L) for the combustion chamber. However, a distinct peak also exists at approximately 8.1 kHz frequency. This frequency is believed to be the vortex shedding frequency generated from the LOX post recess region.

Simulations were conducted using the DLR injector grid with constant inlet mass flow rate, constant outflow pressure, and viscous wall boundary conditions. The values used for the mass flow rate and inlet temperature were discussed earlier, and the outflow and chamber supercritical pressure was set to a value of 81.54 atm (1200 psia). The code was initiated by running in steady-state mode for 20,000 time steps, and it was then restarted using time-accurate analysis for another 600,000 time steps, using Δt of $1e-7$ s, which is equivalent to 60 ms of physical time.

Mass flow rate and pressure probe readings inside the LOX tube reveal a dominant frequency of 8.1 kHz. This frequency pervades throughout all the probe readings inside the LOX post recess region. At the injector exit plane, the 8.1 kHz frequency still remains the dominant frequency with the addition of a few stronger frequencies at 4, 5.9, and 7.1 kHz, as presented in Fig. 7. This frequency corresponds exactly to the 8.1 kHz frequency presented in the PSD plot of chamber pressure and is believed to be the vortex shedding frequency from the LOX post recess region, as shown in Fig. 6. It is also interesting that the cold flow calculation shows activity near 4 and 6 kHz that were attributed to chamber longitudinal acoustic modes. Since there is no combustion in our calculations, the presence of these frequencies are attributed solely to hydrodynamic interactions within injector flow passages. The 4 kHz mode could be a subharmonic of the main post shedding frequency. Clearly, more work is required here to better understand how these modes appear.

IV. Overview of Injector Geometry

Most liquid rocket engine injectors in operation today are connected to an upstream manifold assembly via drilled passages, and they do not make use of a cavitating venturi in order to maintain constant mass flow rates. The liquid rocket engine manifold is maintained at constant ullage pressure, which is typically supplied either by a turbopump system or a pressure-regulated propellant tank assembly. The injector feed lines and passage dimensions are designed to deliver the designated propellant mass flow rates to the engine by incurring a 15–25% pressure drop across the injector assembly. For this reason, oxidizer and fuel manifold assemblies were modeled using constant backpressure conditions. Removal of the constant mass flow rate inlet condition allows the system to operate in more degrees of freedom. The mass flow rate is now free to fluctuate to accommodate the incurred pressure drop and the inherent dynamics of the injection process. The instantaneous mass flow rate is now affected by the complex vortex shedding dynamics and pressure fluctuations, which may be taking place in the LOX post recess and injector faceplate regions. Also, chamber pressure fluctuations due to combustion may travel upstream and affect the overall resistance of the system, thus causing additional perturbations in the mass flow rate history.

The baseline injector geometry is modeled after the hydrogen/oxygen multielement experimental bipropellant liquid rocket engine, which was hot-fire tested in 2007 and 2008 as shown in Fig. 8 [20]. The Loci/CHEM code was used to perform single-element axisymmetric, unsteady, nonreacting CFD simulations on a single coaxial injector element.

The computational domain models the LOX and GH_2 manifolds, the LOX post, the GH_2 annulus, the LOX recess region, and half the length of the combustion chamber, as shown in Fig. 9. Constant inlet pressure boundary conditions were specified for the LOX and GH_2 manifolds. The feed lines were all modeled as viscous walls, implementing the no-slip boundary condition for modeling viscous boundary layers. To achieve accurate solutions, the grid was stretched to achieve a normal grid spacing of $y^+ \sim 1$. The no-slip

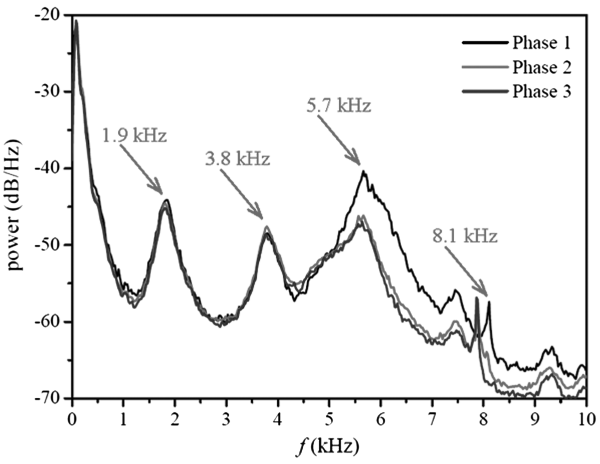

Fig. 6 PSD plot from chamber pressure measurements at supercritical pressure $r = 0.67 d_i$, $do = 7.4$ mm [6].

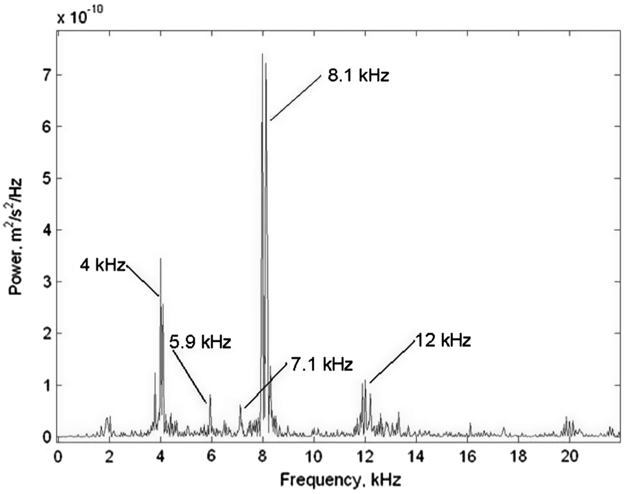

Fig. 7 PSD of mass flow rate at injector exit plane, x-station 8 R.

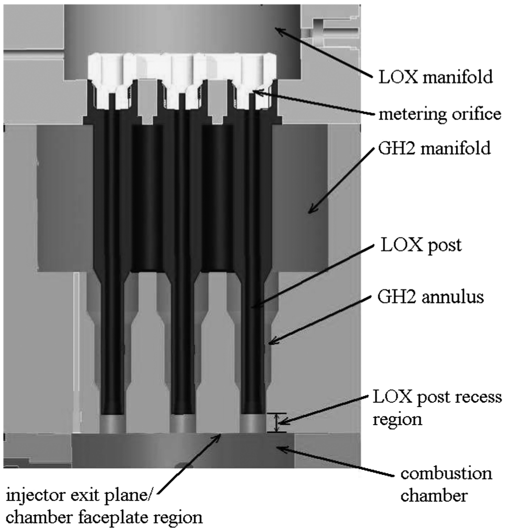

Fig. 8 Close-up view of coaxial injector assembly [6].

boundary condition was also specified at the surface of the injector faceplate. The outer surface of the combustion chamber was modeled with the inviscid wall boundary condition. The entire computational domain is axisymmetric about the centerline of the chamber, and this is reflected in the boundary condition imposed on the lower surface. A total of 58,700 grid points are used in the entire computational domain. To resolve large gradients, the mesh is more populated with grid points in the recess region, while the GH_2 and LOX feed lines are the least populated since the flow is fairly uniform in those regions.

The grid has been nondimensionalized with respect to the diameter of the LOX post D. The dimensions of the entire computational domain are presented in Fig. 10, while the dimensions in the vicinity of the LOX post recess region are presented in Fig. 11. The overall length of the domain is $53.86D$, while the radius of the combustion chamber is $6.9D$. While this is a very large diameter for a single element, we wished to replicate the overall diameter of the hydrogen–oxygen multielement experiment in order to potentially capitalize on some high-frequency measurements made within that chamber. Unfortunately, the transducer that would provide the most insightful data failed during testing. Finally, the length of the recess region is $1.16D$.

For the grid convergence study, the ideal gas model in Loci/CHEM was used to simulate gaseous oxygen and hydrogen flows for a nonreacting case with an O/F ratio of 4.7. A coarse grid (65,000 grid points), an intermediate grid (133,000 grid points), and a fine grid (264,000 grid points) were used in the study to ensure the solution was grid independent. The shedding frequency of the splitter post was computed from the power spectrum of the axial velocity obtained from nine probe points located directly downstream of the splitter post. The 65,000 grid point mesh was deemed acceptable since there was less than 5% deviation in shedding frequency between the fine and coarse grids in the study. More specifically, the shedding frequency between the coarse and fine grids was equal to 15.73 and 15.87 kHz, respectively. In addition, the axial velocity probe point readings reported similar values between the fine and course grids. For more details, please refer to [18].

The entire computational domain was probed at 11 different vertical planes to obtain local integrated mass flow rate histories. In

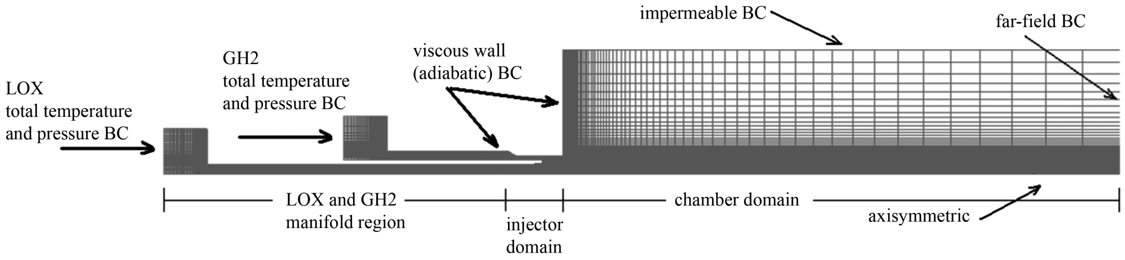

Fig. 9 Grid and boundary conditions (BCs) for LOX/GH_2 bipropellant rocket engine.

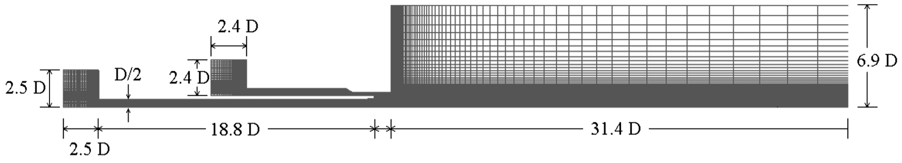

Fig. 10 Nondimensionalization of entire computational domain, where *D* equals LOX post diameter.

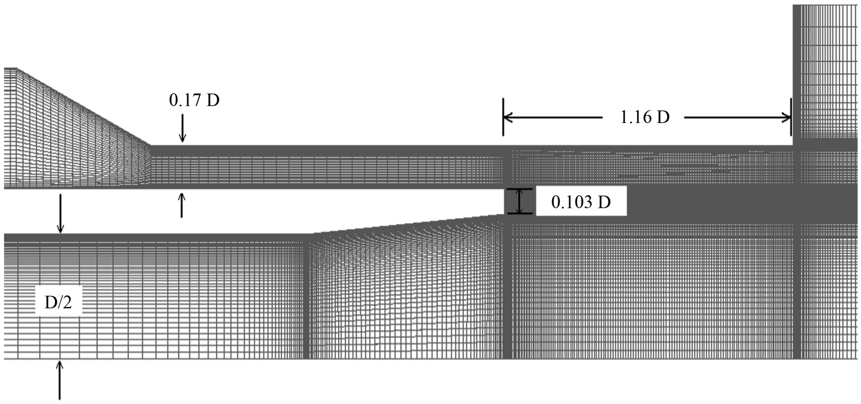

Fig. 11 Nondimensionalization of recess region, where *D* equals LOX post diameter.

addition, pointwise probing was taken at the same axial locations to obtain velocity, pressure, and density measurements inside the flowfield. More specifically, x-stations 1E through 4E are located inside the LOX post, as shown in Fig. 12. X-station 5E is located inside the recess region, while stations 6E through 11E lie inside the combustion chamber region. Similarly, probe points 0 through 2 are located inside the feed lines, point 3 lies inside the recess region, and probe points 4 through 9 are located inside the combustion chamber region, as shown in Fig. 13. Since most of the hydrodynamic activity occurs inside the LOX post recess region, 10 vertical x-stations were probed in its vicinity to obtain integrated mass flow rate measurements (shown in Fig. 14). X-stations 1 through 3 R are located inside the LOX post, while x-station 4 R is located at the plane of the LOX post tip. X-stations 5 through 7 R are located inside the LOX post recess region, while x-station 8 R lies at the injector exit plane. Stations 9 and 10 R are located inside the chamber region, just downstream of the injector exit plane. In addition, probe point 10 is located at the LOX post tip plane, while probe points 11 and 12 are located at the injector exit plane. All probe points except probe point 12 are located at half the radius of the LOX post, as shown in Fig. 13.

V. Baseline Injector Simulation

The baseline simulation employed a constant LOX manifold pressure of 1277 psia (86.92 atm) and a constant GH_2 manifold pressure of 1345 psia (91.53 atm), while the outflow boundary condition employed a constant chamber pressure of 1200 psia (81.66 atm). These simulations were run for more than 50 ms of physical time ($\Delta t = 1e - 7$ s) in an unsteady mode (six Newton and four Gauss–Seidel iterations) using the SST turbulence model [12]. For these runs, the average O/F ratio is equal to 10.3, the fuel/oxidizer (F/O) momentum ratio is 2.3, and the F/O velocity ratio is 19.0. The LOX and GH_2 inlet temperature was kept at a constant 85 and 285 K, respectively. The LOX stream had an average post tip inlet velocity of 21.4 m/s ($Re = 60,200$), a Mach number of 0.014, and a density of 1187 $\mathrm{kg/m^3}$, while the GH_2 fuel annulus inlet velocity was much higher, reading at 407 m/s ($Re = 168,800$), a Mach number of 0.29, and an injection density of 7.4 $\mathrm{kg/m^3}$. For most of the runs, the Hirschfelder–Buehler–McGee–Sutton (HBMS) equation of state was used to simulate LOX [20].

The large difference in velocity and density between the LOX and GH_2 streams leads to large shearing forces that promote vortex formation, breakup, and mixing between the two streams. Based on a LOX surface tension σ 0.013 N/m, the Kelvin–Helmholz wavelength ($\lambda = 3\pi\sigma/\rho_g u_g^2$) is roughly 0.1 μ due to the incredible gas phase dynamic pressure imposed on the liquid interface. Because this K–H length scale is so tiny, the mixing field is dominated by vortex formation taking place at the backward-facing step region of the LOX post tip. Figures 15–17 present a snapshot in time of the flowfield at 670,000 time steps (67 ms) from the beginning of its computations. By this time, all of the initial perturbations from the startup transient have been washed out of the computational domain, and the injector, although highly unsteady in nature, is producing semiperiodic vortex formation. In the streamline plot shown in Fig. 16, smooth and steady streamlines exist inside the manifold feed lines up until the LOX post tip where the two fluids come in contact. The mixing process taking place inside the recess region has a profound effect on the overall length of the LOX core, which seems to disappear at approximately the middle of the chamber domain [21]. In this study, the LOX core length is defined as the point where the local oxygen density drops below 25% of the pure LOX density (1187 $\mathrm{kg/m^3}$).

Of critical importance to injector dynamics is the activity taking place inside the narrow LOX post recess region. As shown in a close-up view of Fig. 17, vortices are initially created on the backward-

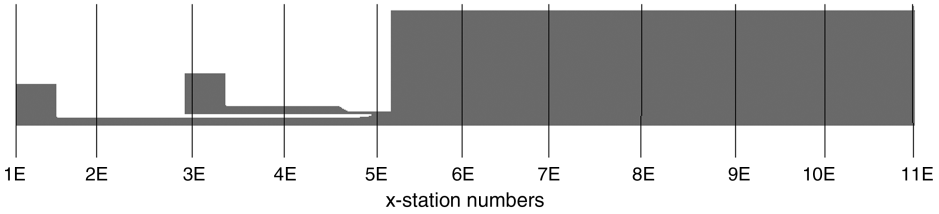

Fig. 12 Entire computational domain mass flow rate integration x-station locations.

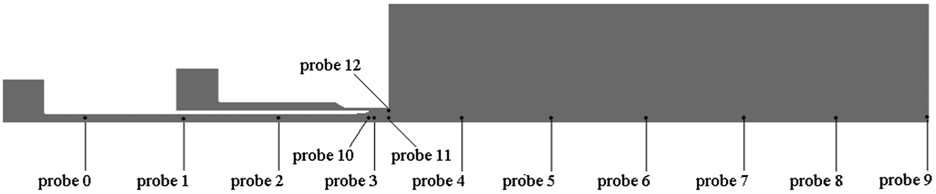

Fig. 13 Entire computational domain probe point locations.

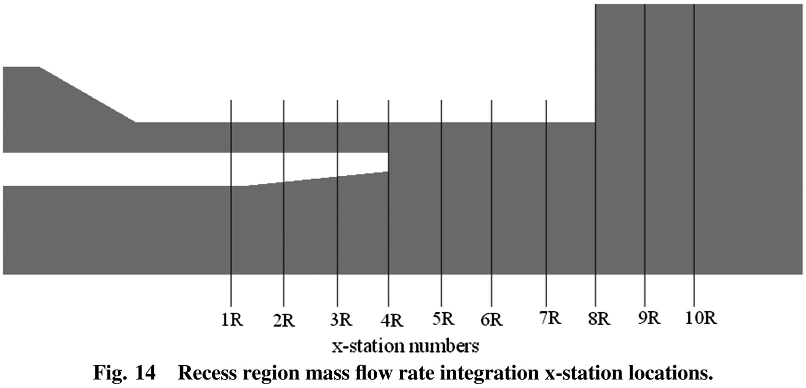

Fig. 14 Recess region mass flow rate integration x-station locations.

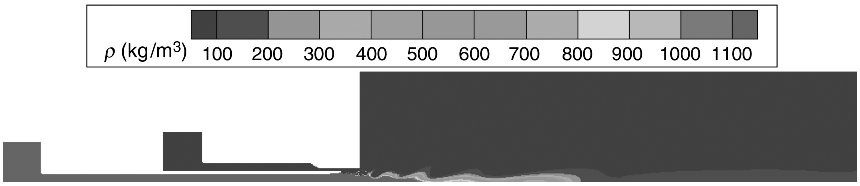

Fig. 15 Density contour plots for entire computational domain at 67 ms.

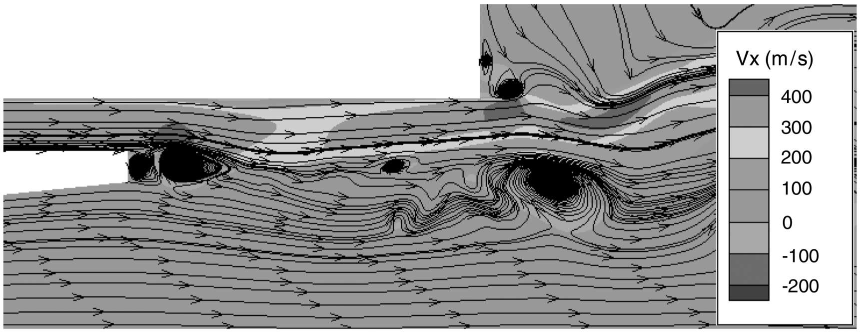

Fig. 16 Close-up view of streamlines inside LOX post recess region at 67 ms.

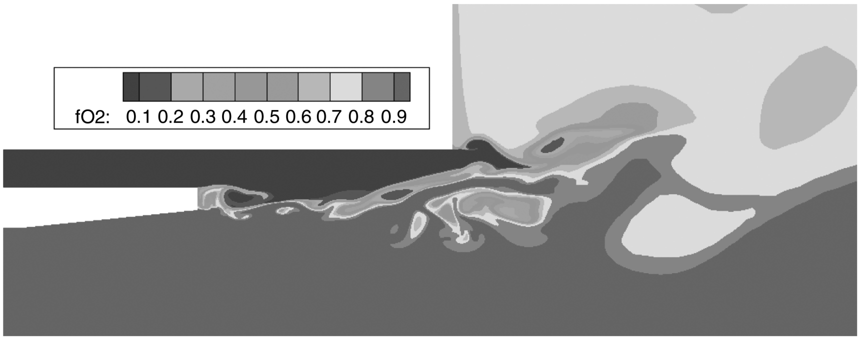

Fig. 17 Oxygen mass fraction in LOX post recess region at 67 ms.

facing step of the LOX post tip. The upper gaseous hydrogen stream produces clockwise-rotating vortices that help induce counterclockwise rotating vortices inside the lower LOX stream. These vortices are carried downstream, whereby shearing action between the two streams creates further breakup of these vortices into smaller entities. Vortex shedding also takes place at the backward-facing step of the chamber faceplate region. These vortices move past the injector exit plane, eventually dissipating further downstream inside the chamber domain.

As mentioned earlier, the mass flow rate was computed at various axial locations inside the computational domain. Starting upstream from inside the LOX post, the mass flow vs time signal is simple and periodic in nature. A single dominant frequency exists at 7.6 kHz, which comes close to the LOX post acoustic frequency of 8.2 kHz ($a/2L$ mode), as shown in the mass flow rate PSD plot in Fig. 18. This frequency is also confirmed from pressure and density pointwise probing inside the LOX post.

Moving further downstream, the next point of interest is the plane of the LOX post tip measured by x-station 4 R and probe point 10. This plane demarcates the beginning of the LOX post recess region, whereby the LOX and GH_2 fluid streams first come into contact with each other. The mass flow and velocity probes exhibit a single dominant frequency of 7.6 kHz, which is identical to the dominant frequency inside the manifold feed line. Further downstream, the LOX and GH_2 fluid streams mix violently inside the injector recess region. Vortices being shed from the post tip region, combined with shearing action created at the interface between the low-speed LOX and high-speed GH_2 streams, create multiple large and small vortical structures. These structures merge, roll, and breakup into complicated and, often, nonrepeatable patterns inside the recess region. Close examination of the movies reveals that clear distinction and tracking of vortices inside the recess region is very difficult, since most of the structures starting at the post tip seldom make it to the

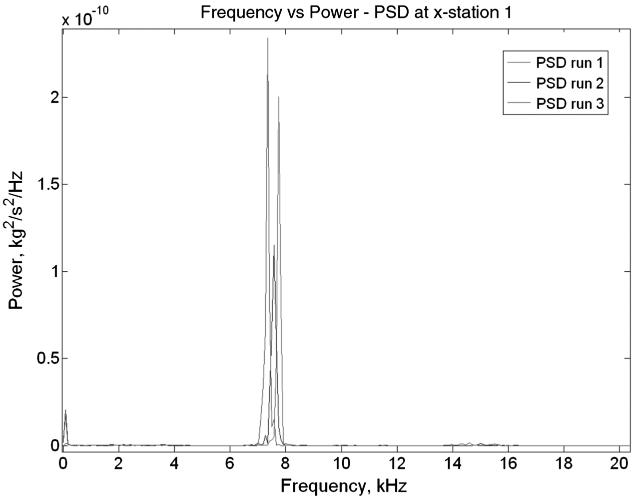

Fig. 18 Mass flow rate PSD plot inside LOX manifold feed line (x-station 3 R).

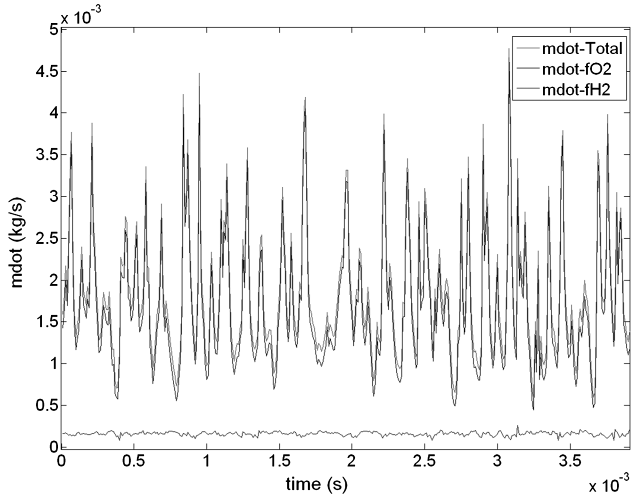

Fig. 19 Mass flow rate vs time at injector exit plane (x-station 8 R).

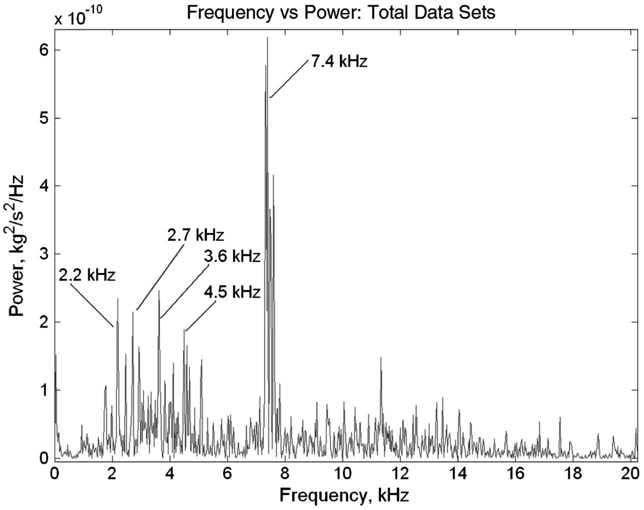

Fig. 21 PSD of mass flow rate for three combined runs at injector exit plane (x-station 8 R).

injector exit plane while still preserving their initial size and shape. A vortex shedding from the post tip will most likely end up merging and breaking apart with nearby vortices multiple times while traversing the 5.7-mm-long recess region. The complexity of the flowfield is evident in the PSD plots of integrated mass flow, axial velocity, density, and pressure. In contrast to the simple, distinct, and repeatable frequency content of the LOX post, the PSD plot of the recess region shows a very broadband frequency spectrum that spans from a few hertz to over 30 kHz. In addition to the numerous frequencies being present, the top 10 strongest frequencies often have power levels that are of the same order of magnitude and very close to one another, thus making it difficult to distinguish between the strongest frequencies.

At the injector exit plane (x-station 8 R), the mass flow rate is plotted versus time in Fig. 19. Violent pulsations are present in all three flows as a result of the strong interaction of vortical structures emanating from the LOX post tip. As expected, due to an average O/F ratio of 10, the LOX mass flow rate dominates the picture. Figure 20 shows the PSD plot of the integrated mass flow rate for three consecutive 15 ms runs. The run-to-run variability is telling of the complex and highly unsteady nature of the flowfield inside the recess region. However, the 7.4 kHz frequency is dominant for all three of these runs. The PSD of the combined data (45 ms) is presented in Fig. 21, whereby the dominant frequencies, in descending order, are 7.4, 3.6, 2.2, 2.7, and 4.5 kHz. In addition to the integrated mass flow, pointwise probing of the flowfield reveals a few interesting observations. Probe 11, which is located closer to the centerline, is immersed more inside the LOX region, while probe 12, which is located directly above and closer to the outer wall, is immersed more inside the GH_2 flowfield. Consequently, the probe closest to the slower-moving LOX stream is picking up (in addition to the 7.4 kHz) dominant frequencies for velocity, density, and pressure in the lower frequency range (2.1—2.8 kHz), while the probe closest to the faster-moving GH_2 stream is showing more frequency content toward higher frequencies (above 7.4 kHz). Of course, most of these frequencies are also evident in the integrated mass flow, but the gaseous side probes have a propensity to pick up more of the higher frequencies. Since the gaseous stream is two orders of magnitude faster than the liquid stream, the ensuing gas vortex shedding frequency is higher than the liquid, which may help explain this observation. This trend is evident in most of the simulations.

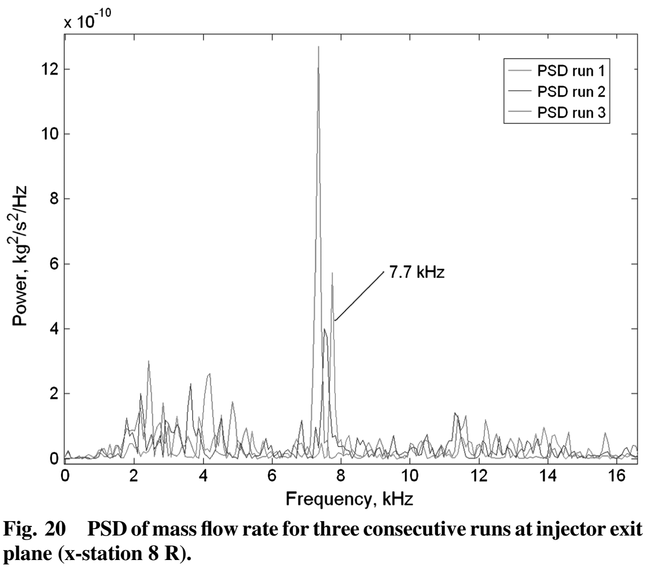

Fig. 20 PSD of mass flow rate for three consecutive runs at injector exit plane (x-station 8 R).

As we move from the close confines of the recess region into the large volume of the combustion chamber domain, the flow now has the capability to expand outward. The vortical structures that emanate from the recess region and shed off the injector faceplate have the propensity to merge with each other, forming larger, slower-moving vortices. These large vortices merge further with neighboring vortical structures as they gradually convect downstream into the chamber domain. This phenomenon is evident from both the movies and PSD plots. Located just 2.2 mm downstream of the injector exit plane is x-station 6E and probe point 4, as shown in Figs. 12 and 13. At this location, vortex merging has already taken place and the measured frequencies are significantly lower. The

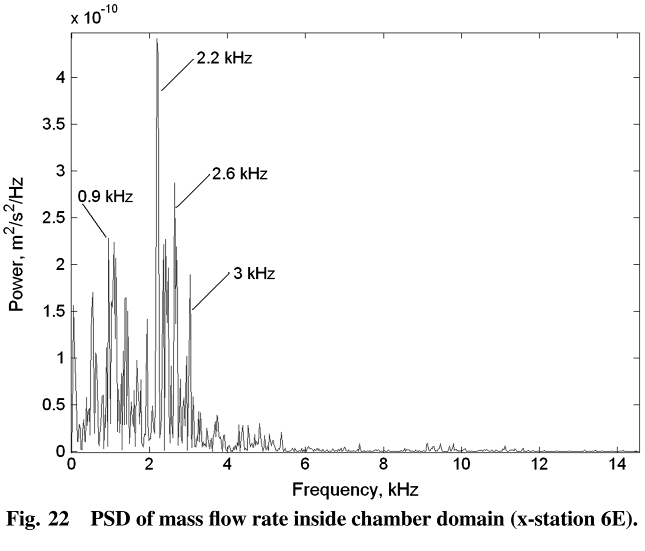

Fig. 22 PSD of mass flow rate inside chamber domain (x-station 6E).

dominant frequency is 2.2—2.6 kHz for mass flow (as shown in Fig. 22) and 2.4 kHz for the velocity probe at this location. Similar frequencies are showing up in the density and pressures probes. Most activity is happening in the low-frequency range of 0.9—2.7 kHz, with very little activity happening beyond 6 kHz.

The nine images in Fig. 23 depict the PSD plots across the entire recess region (x-stations 2—10 R). As discussed in the previous sections, the emergence of additional strong frequencies (besides LOX post acoustic mode at 7.4 kHz) is obvious as we gradually move downstream through the injector passages. In the recess region, the overall trend shows the emergence of a lower frequency band primarily ranging between 2.2 and 4.7 kHz. This frequency band is obvious in all locations downstream of x-station 5 R. The most commonly occurring frequencies in this band are the 2.7 and 3.6 kHz. The 3.6 kHz frequency, which is the second strongest frequency (after the 7.4 kHz) inside the recess region, is attributed to vortex shedding from the LOX post tip. Inside the chamber region (x-station 6E), the 2.2 and 2.6 kHz frequencies become the most dominant, while the 7.4 kHz frequency completely disappears. The coexistence of the 2.6 kHz frequency at the chamber faceplate region (stations 8—10 R) and the region located 22 mm inside the chamber (x-station 6E) seem to indicate that this frequency is predominantly caused by vortex shedding from the injector faceplate region. It is interesting to note that further downstream inside the chamber, the large vortices dissipate almost entirely and low frequencies of 0.6 kHz now dominate the spectrum.

In addition to the dominant frequencies produced by injector hydrodynamic interactions, the mass flow rate pulsations are also of great interest to injector designers. Mass flow rate histories were plotted for three consecutive 15 ms runs to assess the evolution of the pulsations as one travels downstream inside the injector computational domain. More specifically, the standard deviation relative to the average mass flow rate is presented in Fig. 24 for x-stations located inside the LOX post and post recess region (x-station 1—10 R). As shown in this plot, the relative standard deviation inside the LOX post (x-stations 1–4 R) is equal to approximately 12% with respect to the average mass flow rate of 0.00172 kg/s ($2e-4$ kg/s standard deviation). Inside the injector recess region (x-stations 4–8 R), we notice a sharp rise in pulsations (12 to 47% relative standard deviation). As we move from the recess region into the chamber, the pulsations begin leveling off (x-stations 8–10 R) as the gas expands into the chamber. Close comparison between the recess region and the entire domain reveals that maximum pulsations occur somewhere between x-station 8 R and x-station 6E (3–22 mm downstream of the injector exit plane), approximately where most combustion activity should be taking place. Toward the end of the chamber domain, the pulsations level off to approximately 23%.

VI. Effects of Oxidizer-to-Fuel Ratio Variation

The effect of varying the oxidizer-to-fuel ratio is of great importance to designers of liquid rocket propulsion systems. Using

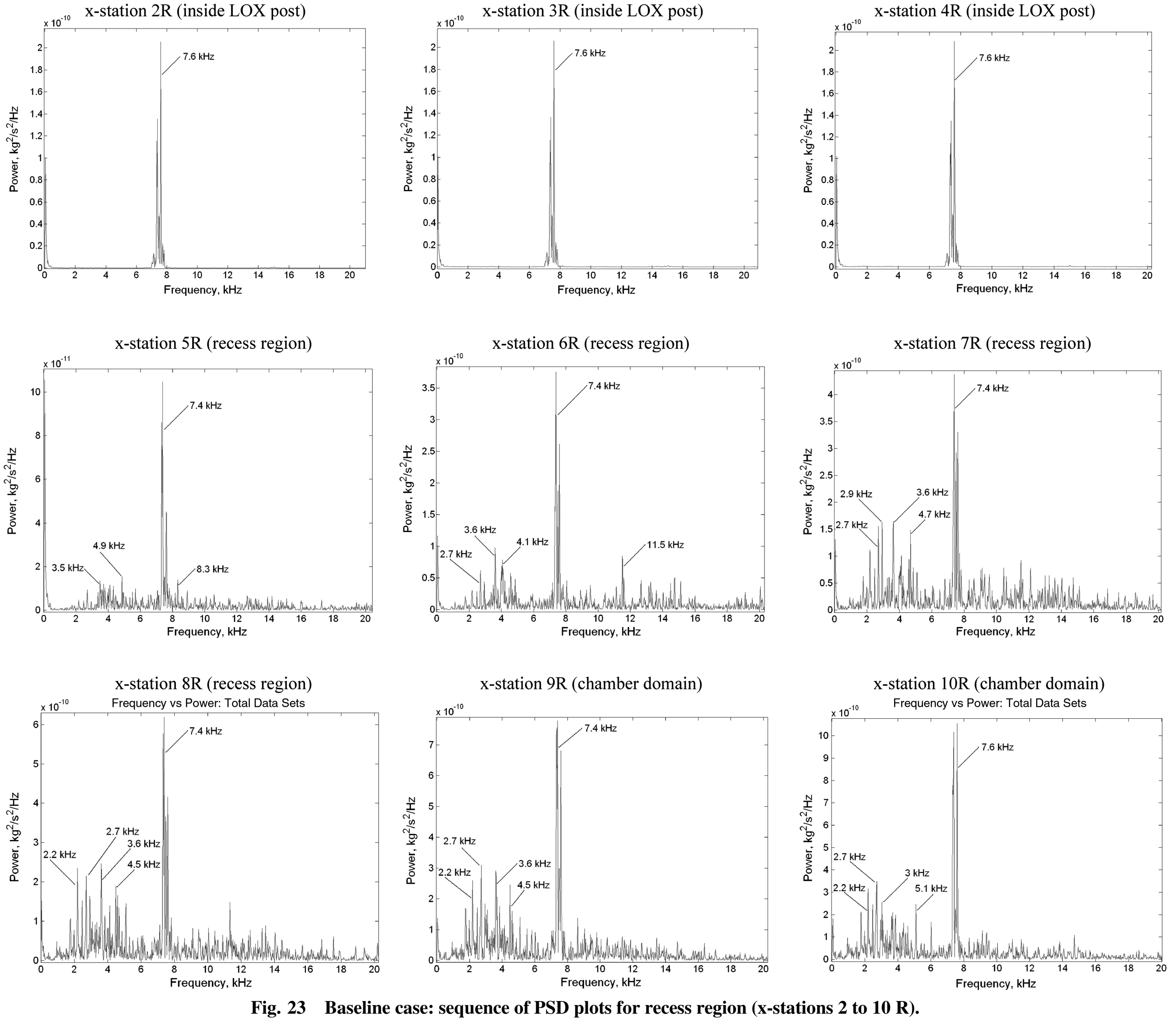
x-station 2R (inside LOX post)

x-station 3R (inside LOX post)

x-station 4R (inside LOX post)

x-station 5R (recess region)

x-station 6R (recess region)

x-station 7R (recess region)

x-station 8R (recess region)

Frequency vs Power: Total Data Sets

x-station 9R (chamber domain)

x-station 10R (chamber domain)

Frequency vs Power: Total Data Sets

Fig. 23 Baseline case: sequence of PSD plots for recess region (x-stations 2 to 10 R).

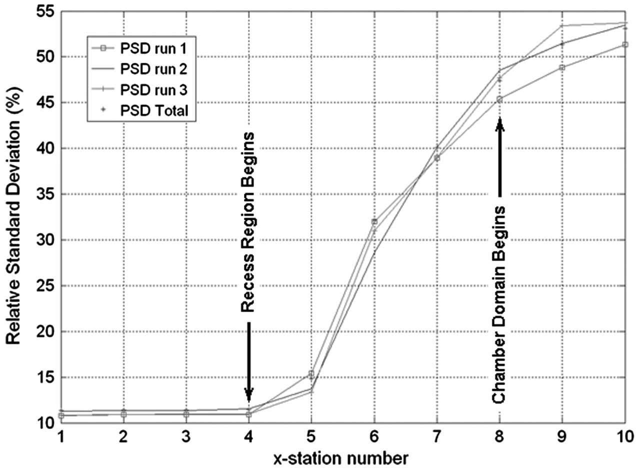

Fig. 24 Mass flow rate fluctuations vs x-station location inside baseline injector recess region (x-stations 1–10 R).

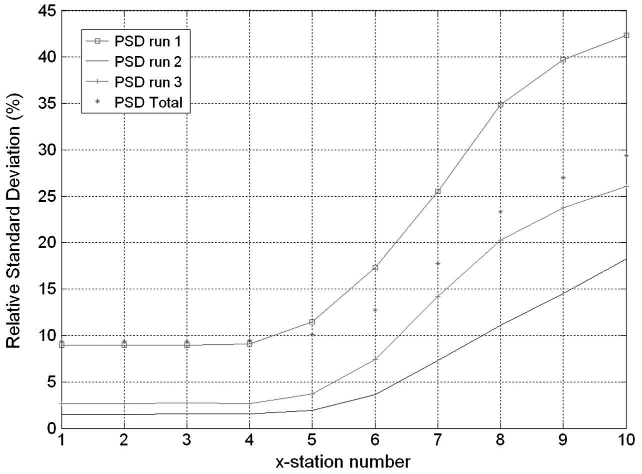

Fig. 25 Mass flow rate fluctuations for high O/F case (F/O momentum ratio = 0.6) inside recess region (x-stations 1 to 10 R).

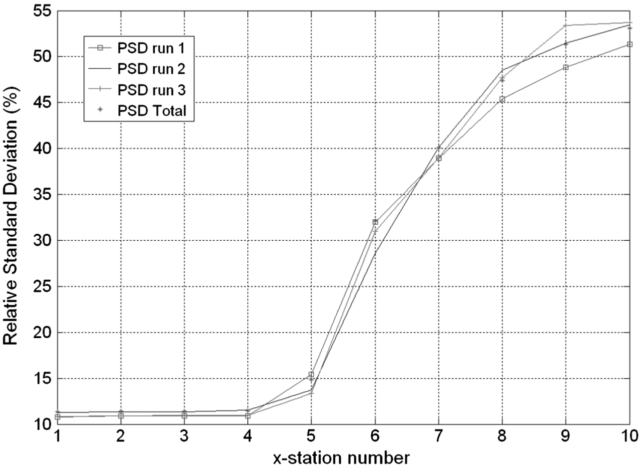

Fig. 26 Mass flow rate fluctuations for baseline case (F/O momentum ratio = 2.3) inside recess region (x-stations 1 to 10 R).

the baseline injector geometry, low and high O/F ratio cases were simulated and postprocessed for analysis. The GH_2 fuel manifold stagnation pressure remained at a constant 1344 psia (91.5 atm), while the LOX manifold stagnation pressure was varied in order to change the LOX mass flow rate and, consequently, the O/F ratio. As shown in Table 2, the LOX manifold pressure was varied between 1239 psia (84.3 atm) and 1355 psia (92.2 atm), leading to O/F ratios of 3.4, 10.3, and 19.6 for low, baseline, and high oxidizer mass flow cases, respectively. The respective F/O momentum ratios are equal to 0.6, 2.3, and 12.1. The fuel injection velocity at the LOX post tip plane varied between 385 and 437 m/s (Mach 0.29–0.41), while the LOX inlet velocity varied between 8.8 and 44 m/s (Mach 0.007–0.03).

As shown in previous injector studies with the constant mass flow inlet conditions, the high F/O momentum ratio case (O/F = 3.4) creates larger vortices that promote more mixing and dissipation of the LOX stream [6]. Consequently the LOX core length becomes shorter with decreasing O/F ratio (increased F/O momentum ratio). Moreover, probing inside the computational domain reveals that an increase in F/O momentum ratio also leads to increased amplitude of the mass flow fluctuations. This is evident in Fig. 25, where the relative standard deviation in mass flow rate at the injector exit plane for the low F/O momentum ratio of 0.6 is approximately equal to 27% of the mean mass flow rate. As shown for the baseline case (F/O momentum ratio of 2.3) in Fig. 26, fluctuations reach approximately 47%, while for the high F/O momentum ratio shown in Fig. 27, they are equal to approximately 84%. Flow fluctuations remain fairly constant inside the LOX post (x-stations 1–4 R), while they begin growing inside the recess region, reaching a maximum value just past the exit plane (x-station 8 R) and tapering off thereafter.

Table 2 Operating conditions for high and low oxidizer mass flow rate variations

	High Ox	Baseline	Low Ox
GH_2 manifold, Pressure,. atm	91.5	91.5	91.5
GH_2 manifold, temperature, K	285	285	285
LOX manifold, pressure, atm	92.2	86.9	84.3
LOX manifold, temperature, K	85	85	85
At LOX post tip region			
O/F ratio	19.6	10.3	3.4
F/O momentum ratio	0.60	2.3	12.1
F/O velocity ratio	9.9	19.0	43.7
LOX: oxidizer			
Injection mass flow rate, kg/s	1.218	0.581	0.197
Injection velocity, m/s	44	21.4	8.8
Injection Mach number	0.03	0.014	0.007
Injection density, kg/m^3	1,187	1,187	1,187
Reynolds number	124,000	60,200	24,800
Gaseous hydrogen: fuel			
Injection mass flow rate, kg/s	0.062	0.056	0.059
Injection velocity, m/s	437	407	385
Injection Mach number	0.41	0.29	0.354
Injection density, kg/m^3	7.25	7.5	7.5
Reynolds number	176,342	168,800	160,600

The effect of varying the O/F ratio (by varying LOX mass flow rate) on injector frequency response is examined next. The dominant frequency inside the LOX post is very close to its acoustic frequency of ~8.2 kHz ($a/2L$ mode). At the injector exit plane, the dominant frequency decreases as the O/F ratio becomes smaller, as shown in Fig. 28. This is caused by a decrease in LOX velocity, which dominates the flow due to its density being two orders of magnitude greater than gaseous hydrogen. The low O/F ratio case exhibits strong activity in the 3–6 kHz range due to the lower velocity LOX moving through the injector recess region. The 3.8 and 5.1 kHz frequency is relatively the strongest, with activity also occurring in the 9–10 kHz range, as shown in Fig. 28. However, the corresponding increase in F/O momentum ratio produces more diverse vortical structures, which create PSD plots of increasing complexity and multiple high-power frequencies.

On the other hand, the high O/F ratio case exhibits a high-frequency region between 13–16 kHz, with relatively strong frequencies at 14.5 and 13.4 kHz, as shown in Fig. 29. For this case, a weaker, lower frequency band is also present in the vicinity of 3 kHz. It is interesting to note that the power at 8.2 kHz frequency relative to the high-frequency band fluctuates continuously between x-stations 6 and 10 R. In some instances, 8.2 kHz is relatively the strongest, while in others, it becomes the second strongest. The

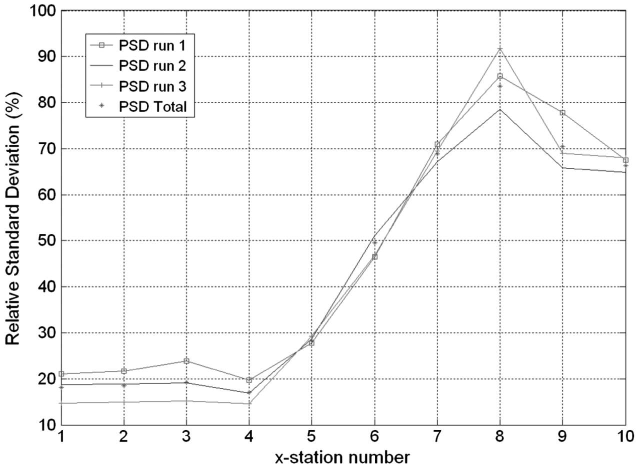

Fig. 27 Mass flow rate fluctuations for low O/F case (F/O momentum ratio = 12.1) inside recess region (x-stations 1 to 10 R).

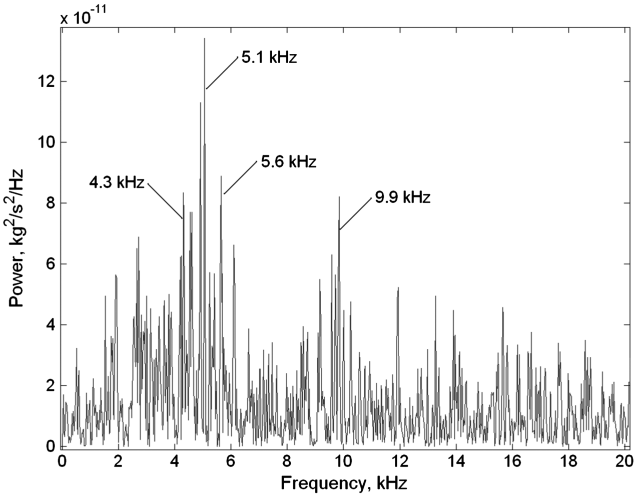

Fig. 28 PSD of mass flow rate for low O/F ratio case at injector exit plane (x-station 8 R).

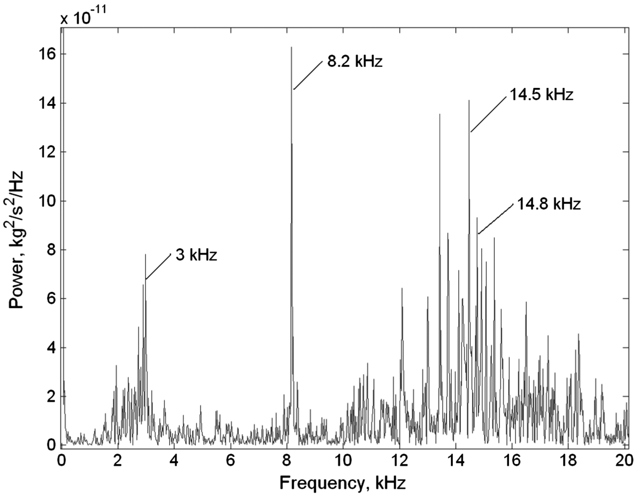

Fig. 29 PSD of mass flow rate for high O/F ratio case at injector exit plane (x-station 8 R).

fluctuation in relative power between a few frequency bands inside the recess region is a recurring phenomenon that is observed in many other cases throughout this study.

As mentioned previously, the high-power frequencies for the probe closest to the gaseous stream (probe 12) are higher in frequency than those picked up by the probe closest to the liquid stream (probe 11). Of course, most of these frequencies are also evident in the integrated mass flow, but the gaseous side probes have a propensity to pick up more of the higher frequencies. Since the gaseous stream is two orders of magnitude faster than the liquid stream, the ensuing gas vortex shedding frequency is higher than the liquid, which may help explain this observation. It must be noted that, inside the LOX stream (probe 11), the frequency spectrum for the density and pressure probes is almost identical in its distribution of power. However, the similarity between the density and pressure spectrums is not evident inside the GH_2 stream (probe 12). This observation is again attributed to the difference in probe location. The probe located primarily inside the liquid stream (probe 11) will exhibit a more closely coupled pressure/density relationship than the probe located mostly inside the gaseous stream (probe 12).

VII. High and Low Fuel Mass Flow Rate Variations

In the previous section, the fuel manifold stagnation pressure was kept constant, while the oxidizer manifold pressure was varied. In this next set of simulations, the oxidizer manifold pressure remains at its constant baseline value of 1277 psia (86.92 atm), while the fuel manifold pressure is varied from its baseline value of 1345 psia (91.53 atm) to a high of 1390 psia (94.53 atm) and a low of 1272 (86.53 atm). The variation in manifold stagnation pressure leads to high and low gaseous hydrogen inlet mass flow rates that affect the overall O/F and momentum ratios. The low fuel, baseline, and high fuel cases are summarized in Table 3.

Mass flow rate fluctuations in the recess region are compared in Figs. 30 and 31. The low fuel plots show fluctuations of approximately 25% with respect to the mean (Fig. 30), while the high fuel plots show fluctuations of approximately 50% at the injector exit plane (Fig. 31). As expected, the lower fuel inlet mass flow rates (low F/O momentum ratios) lead to less severe mixing between the two streams, thus leading to lower mass flow pulsations. Conversely, the higher fuel inlet mass flow rates lead to higher pulsation levels.

The dominant frequency inside the LOX post is equal to 8.1 and 7.7 kHz for the low and high fuel mass flow cases, respectively. The overall trend at the injector exit plane is for the low fuel mass flow case to produce frequencies lower than those produced by the high fuel mass flow simulations. The low fuel case, which produces the highest O/F ratios, consequently leads to the overall highest frequencies due to the dominance of the oxidizer mass flow rate. Close inspection of the low fuel PSD plots of mass flow inside the recess region reveal that downstream of x-station 5 R, two distinct

Table 3 Operating conditions for Low, baseline, and high fuel mass flow rate variations

	Low fuel	Baseline	High fuel
GH_2 manifold, pressure, atm	86.53	91.5	94.53
GH_2 manifold, temperature, K	285	285	285
LOX manifold, pressure, atm	86.92	86.9	86.92
LOX manifold, temperature, K	85	85	85
At LOX post tip region			
O/F ratio	19.8	10.3	8.0
F/O momentum ratio	0.64	2.3	3.2
F/O velocity ratio	10.3	19.0	22.7
Oxidizer			
Injection mass flow rate, kg/s	0.802	0.581	0.526
Injection velocity, m/s	31	21.4	19.6
Injection Mach number	0.02	0.014	0.013
Injection density, kg/m^3	1,187	1,187	1,187
Reynolds number	87,400	60,200	55,200
Fuel			
Injection mass flow rate, kg/s	0.040	0.056	0.066
Injection velocity, m/s	320	407	446
Injection Mach number	0.3	0.29	0.43
Injection density, kg/m^3	7.1	7.5	7.3
Reynolds number	126,500	168,800	181,000

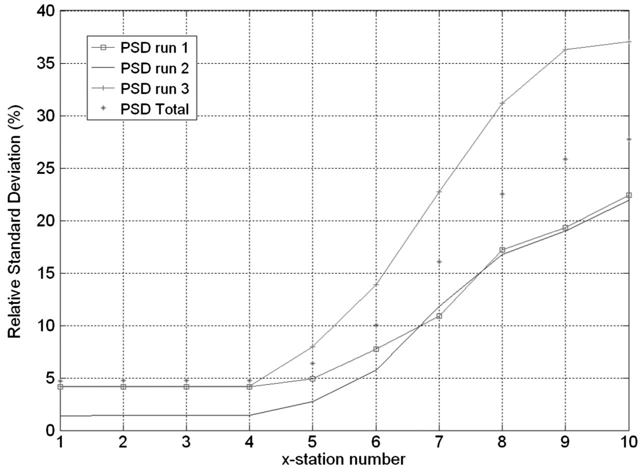

Fig. 30 Mass flow rate fluctuations vs x-station for low fuel case in recess region (x-stations 1–10 R).

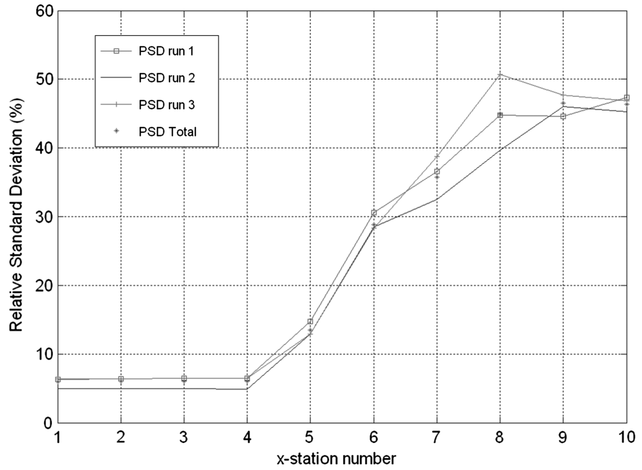

Fig. 31 Mass flow rate fluctuations vs x-station for high fuel case in recess region (x-stations 1–10 R).

bands of frequencies begin to emerge. Namely, the 8.1 kHz natural feed line frequency and the 10.5 kHz frequency are the two strongest frequencies in the recess region. The high-frequency band spans between 10.5 and 11.4 kHz, as shown in Fig. 32. In contrast, the high fuel PSD plot is more broadband and contains more complicated frequency content in comparison with the low fuel mass flow case. The higher F/O momentum ratio creates multiple frequencies, which consequently make it more difficult to pick out the most dominant. A low-frequency band between 2 and 5 kHz seems to be the strongest, but it is closely followed by the surrounding frequency bands, as shown in Fig. 33.

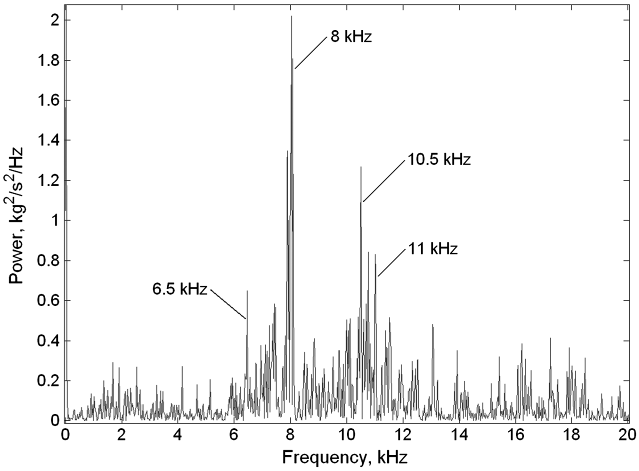

Fig. 32 PSD of mass flow rate for low fuel case at injector exit plane (x-station 8 R).

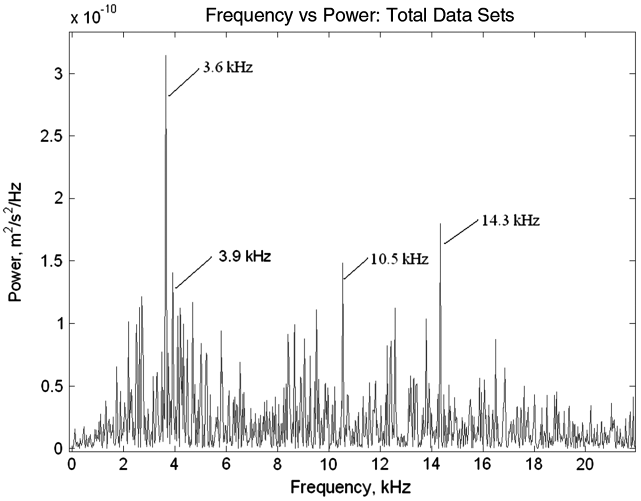

Fig. 33 PSD of mass flow rate for high fuel case at injector exit plane (x-station 8 R).

VIII. Effect of Liquid Oxygen Post Thickness Variation

The thickness of the LOX post tip is an important design variable for liquid rocket coaxial injectors. The design of the post depends on structural as well as heat transfer characteristics. In most instances, the LOX post tip acts as a flame holder due to the recirculation regions created near the backward-facing step where the combustion zone can attach itself. Consequently, the LOX acts to cool the tip of the post and prevent it from melting. A thinner post helps with the cooling process but puts a burden on the structural design. This section aims to shed light on the fluid mechanic effects of varying the post thickness. The effect of post thickness on shedding frequency and injector response are issues that need to be investigated in more detail. Toward this end, an injector with half and two times the baseline thickness was simulated and compared with the baseline case. For this study, the oxidizer and fuel manifold stagnation pressures and O/F ratios were kept constant. To maintain identical F/O momentum and velocity ratios, the cross-sectional areas of both fluid streams were kept constant. This led to a wide recess region for the thick-post case and a smaller recess region for the thin-post case. Consequently the pressure drop across the recess region decreased for the thicker post case, leading to higher oxidizer and fuel mass flow rates (shown in Table 4).

After running the three thicknesses for over 50 ms (500,000 time steps), the pulsation levels at the recess region were compared for all three cases and were found to have very small differences with each other. Comparisons of the thin, baseline, and thick posts show that pulsation levels vary from approximately 5% inside the feed line up to 50% at the injector exit plane. The pulsation levels across the entire domain are also very similar for all three cases.

For the thick-post case, the LOX post mass flow, axial velocity, density, and pressure PSD plots all pick up a single dominant frequency between 7.6 and 8.0 kHz, which corresponds to the natural frequency of the LOX post. At the injector exit plane location, the thick-post case reveals a dominant frequency of 4.1 kHz and a low-frequency band located between 2.5 and 5 kHz. The larger step size of the thick LOX post creates larger vortices that consequently shed at lower frequencies. These lower shedding frequencies are relatively stronger than the LOX post natural frequency and, consequently, dominate the frequency spectrum downstream of x-station 5 R all the

Table 4 Operating conditions for thin and thick LOX post cases

	Thin post	Baseline	Thick post
GH_2 manifold, pressure, atm	91.5	91.5	91.5
GH_2 manifold, temperature, K	285	285	285
LOX manifold, pressure, atm	86.9	86.9	86.9
LOX manifold, temperature, K	85	85	85
At LOX post tip region			
O/F ratio	10.7	10.3	10.1
F/O momentum ratio	1.63	2.3	1.94
F/O velocity ratio	15.7	19.0	17.5
Oxidizer			
Injection mass flow rate, kg/s	0.551	0.581	0.670
Injection velocity, m/s	20.7	21.4	24.9
Injection Mach number	0.011	0.014	0.007
Injection density, kg/m^3	1,187	1,187	1,187
Reynolds number	29,200	60,200	140,200
Fuel			
Injection mass flow rate, kg/s	0.051	0.056	0.066
Injection velocity, m/s	326	407	436
Injection Mach number	0.29	0.29	0.354
Injection density, kg/m^3	7.8	7.5	7.5
Reynolds number	70,700	168,800	363,900

way to 10 Rm as shown in Fig. 34. The lower frequency band is also picked up by the axial velocity and density probe measurements (probes 11 and 12) at the injector exit plane. Inside the chamber domain, an additional high-power frequency emerges at 3.7 kHz, presumably from shedding of the injector faceplate region (x-stations 9–10 R). Deeper inside the chamber domain (x-station 6E, probe 4), the vortical structures from the injector exit plane merge into larger, slower-moving vortices of 1.8 kHz frequency and create activity in the 1.2–2.5 kHz range. Further downstream, the frequencies drop more as the vortices dissipate.

The thin-post case creates smaller, higher frequency vortices that are not sufficiently strong enough to overcome the LOX post acoustic frequency of 8.2 kHz. Consequently, the 13.5 and 5.6 kHz frequencies that emerge downstream of x-station 5 R are overpowered by the magnitude of the LOX post acoustic frequency, which dominates all the way to x-station 10 R inside the chamber region, as shown in Fig. 35. The dominance of the 8.2 kHz frequency is also confirmed by the axial velocity, density, and pressure measurements, which are taken at the injector exit plane. Just as we enter the chamber domain, another strong frequency emerges at 2.9 kHz. This 2.9 kHz frequency is also dominant at x-station 6E further inside the chamber, which seems to indicate that it may be tied to vortex shedding from the injector faceplate region. X-station 6 (probe 4) also reveals strong frequencies at 1.9 and 2.6 kHz.

IX. Changes in Liquid Oxygen Post Acoustic Frequency

As shown in all of the preceding cases, the LOX post acoustic frequency plays an important role in shaping the overall injector frequency response. To further investigate the effects of the LOX post acoustic frequency, a short LOX post case was simulated. The length of the GH_2 annulus was kept the same as the baseline, while the LOX post was shortened from $18.8D$ to $11.3D$ (where $D =$ LOX post diameter). All other dimensions and boundary conditions remain the same as the baseline injector described in Sec. III.

For the short LOX post runs, the overall O/F ratio, F/O momentum ratio, and F/O velocity ratio are equal to 12, 1.6, and 16, respectively. Compared with the baseline case, the oxidizer mass flow rate is slightly higher due to the reduced pressure drop caused by the shorter LOX post. Consequently, this leads to a slightly higher O/F ratio and lower F/O momentum and velocity ratios. The mass flow fluctuations (relative standard deviation) for the short LOX post are only slightly lower than the baseline case.

Results show that the shorter LOX post increased the dominant frequency to 13.3 kHz, which comes close to its calculated acoustic frequency ($a/2L$) of 13.7 kHz and is confirmed by the mass flow, velocity, density, and pressure probes. The dominant frequency further downstream at the LOX post tip plane is still equal to 13.3 kHz. However, a lower frequency band is also beginning to emerge with a dominant central peak at 3.5 kHz while also containing additional frequencies in the 1.5–5 kHz range. At the injector exit plane, the dominant frequencies lie in the 11.1–12.6 kHz range, followed closely by the 1.5–5 kHz frequency range, as shown in Fig. 36. The dominant frequency drops to 1–5 kHz deeper inside the combustion chamber (x-station 6E). The 1–5 kHz frequency, which is also present at x-station 10 R, seems to be caused by vortex shedding from the injector faceplate region.

The effect of changing the dominant frequency by altering the LOX sound speed was examined using the baseline injector configuration. The Soave–Redlich–Kwong (SRK) equation of state was used in place of HBMS to calculate the LOX sound speed [22]. At a pressure of 1277 psia (86.92 atm) and a temperature of 85 K, the SRK model yields a LOX sound speed of 887 m/s, which is 95 m/s below the NIST database result of 982 m/s (the HBMS model calculates a sound speed of 1529 m/s). With this new sound speed value, probe measurements inside the LOX post reveal a 4.7 kHz dominant frequency, which corresponds exactly to its calculated acoustic frequency ($a/2L$ mode). This new acoustic frequency is clearly affecting the activity inside the recess region, which is also showing dominant frequencies of 4.7 kHz and a subharmonic of 9.2 kHz at the injector exit plane, as shown in Fig. 37. It should be noted that the 4.7 kHz frequency is potentially more damaging, since it lies closer to typical thrust chamber acoustic modes.

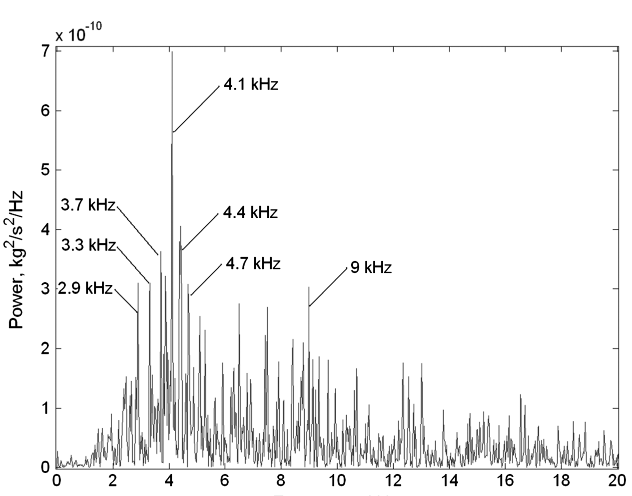

Fig. 34 PSD of mass flow rate for thick-post case at injector exit plane (x-station 8 R).

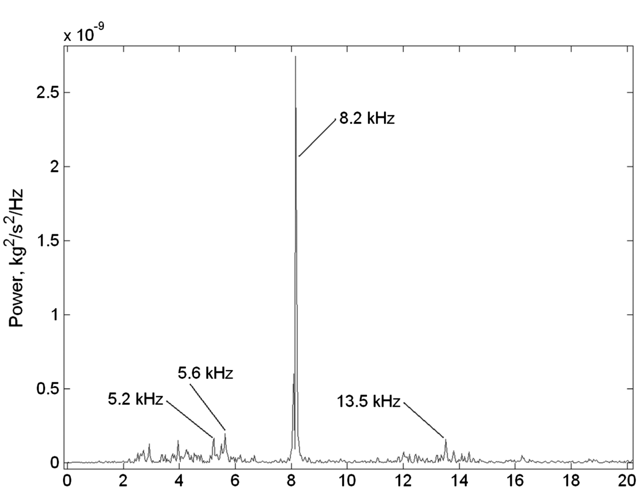

Fig. 35 PSD of mass flow rate for thin-post case at injector exit plane (x-station 8 R).

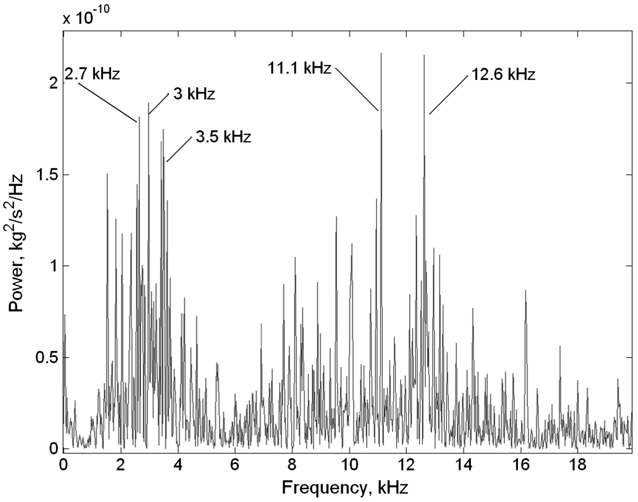

Fig. 36 PSD of mass flow rate for shorter LOX post at injector exit plane (x-station 8 R).

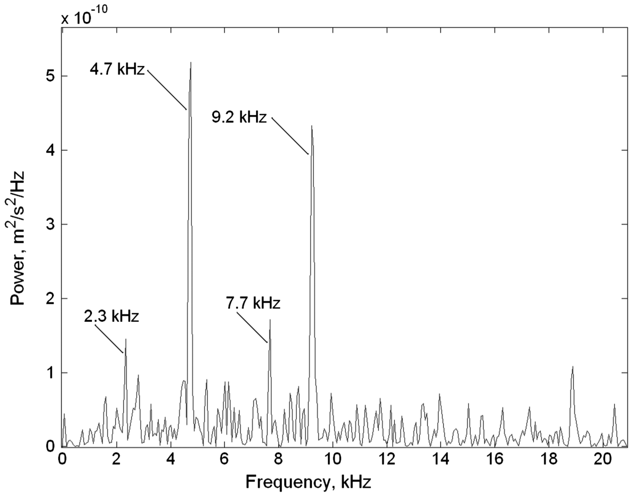

Fig. 37 PSD of mass flow rate using SRK equation of state at injector exit plane (x-station 8 R).

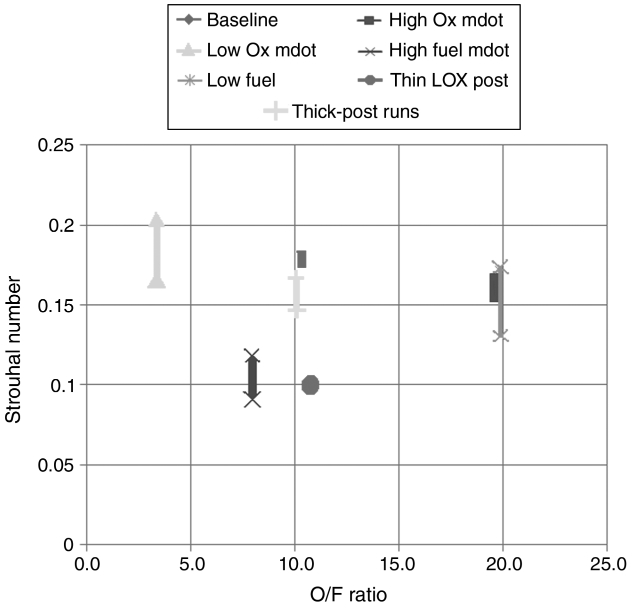

Fig. 38 Strouhal number vs O/F ratio for all real fluids simulations. Strouhal number based on LOX post thickness and LOX injection velocity.

From the preceding simulations, it is evident that the LOX post acoustic frequency had a profound effect on the dominant frequencies created inside the injector recess region. The short LOX post case with the 13.3 kHz acoustic frequency clearly played a role in the formation of the high-frequency band in the 11.1–12.6 kHz range. Moreover, the acoustic frequency of 4.7 kHz from the SRK real fluids model is clearly the dominant frequency up until the injector exit plane. This only helps to emphasize the importance of modeling the correct LOX post geometry and including an accurate real fluids model when dealing with LOX injector studies.

For comparison purposes, the aforementioned simulations were plotted in Strouhal vs O/F ratio and F/O momentum ratio plots. Because of the broadband nature of the PSD plots, the Strouhal number was calculated for a range of dominant frequencies (rather than a single value) based on LOX velocity and LOX post tip thickness. More specifically, the Strouhal vs O/F ratio plot shown in Fig. 38 compares the baseline case with high oxidizer mass flow, low oxidizer mass flow, high fuel mass flow, low fuel mass flow, and thin- and thick-post simulations. The Strouhal numbers are calculated based on the thickness of the LOX post tip and the velocity of the LOX stream at the entrance to the recess region. The O/F ratio range is 3.4–19.8 for this plot. Close examination reveals that, for most of the simulations, the Strouhal numbers lie between 0.13 and 0.2 and exhibit a downward-sloping trend with increasing O/F ratio. Similarly, the same cases show an upward-sloping trend when plotted vs F/O momentum ratio, as shown in Fig. 39. As mentioned in the previous sections of this study, increasing the F/O momentum ratio (or decreasing O/F ratio) leads to more shearing action between

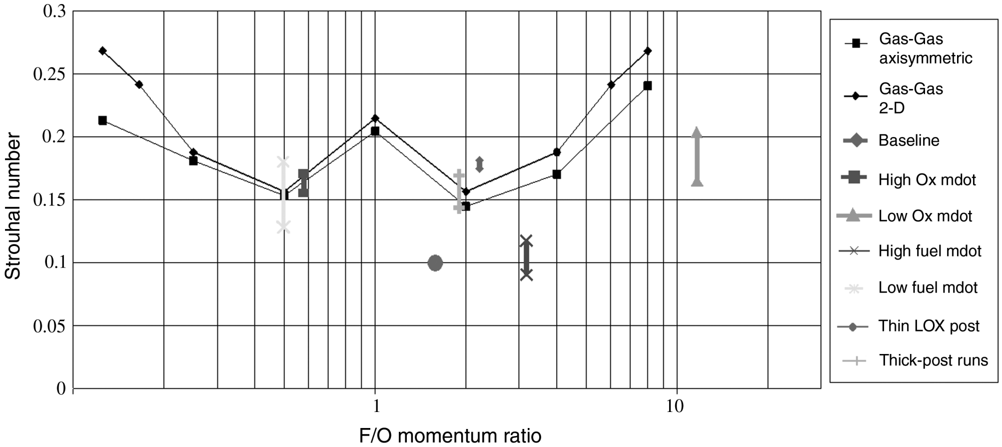

Fig. 39 Strouhal number vs F/O momentum ratio comparisons with gas–gas results from Canino et al. [1,23,24]. Strouhal number based on LOX post thickness and LOX injection velocity.

the two fluid streams, more complicated vortex shedding processes, and overall higher vortex shedding frequencies inside the injector recess region. For this reason, the accompanying upward-sloping trend in Strouhal number vs F/O momentum ratio intuitively makes sense. Moreover, the Strouhal numbers are in very close agreement to gas–gas results by Canino et al., which are included in Fig. 39 for comparison [1,23,24]. In general, the Strouhal numbers for the gas–gas axisymmetric and 2-D cases lie between 0.15 and 0.25, which is in close agreement with the real fluids model results.

There are two results, however, which lie below the range of the aforementioned Strouhal numbers and do not fall in line with the other data. More specifically, the thin LOX post case has a Strouhal number of 0.1 at a F/O momentum ratio of 1.6, which is slightly below the reported range. Despite the decrease in LOX post thickness, the dominant frequency at the injector exit plane is still that of the LOX post acoustic frequency. As mentioned in Sec. VII, the thin-post case creates smaller, higher frequency vortices that are not strong enough to overcome the natural LOX post acoustic frequency of 8.2 kHz, and this consequently throws off the reported Strouhal number.

The high fuel mass flow case reports Strouhal numbers in the 0.09 to 0.11 range, which are also slightly lower than the expected range of Strouhal numbers. However, as shown in Sec. VI, the high fuel mass flow PSD plots are significantly more broadband and complicated in comparison to the low fuel mass flow case. The higher F/O momentum ratio creates multiple frequencies over a wide range, which makes discernment of dominant frequencies more difficult. Consequently, the low-frequency band between 3.6 and 4.5 kHz is relatively close in power to the other neighboring frequencies. The lack of a definitively dominant frequency for the high fuel mass flow case is the best explanation for the Strouhal number deviation.

The Strouhal numbers based on post thickness and LOX injection velocity were also computed inside the chamber domain, at a location downstream of the injector faceplate region (x-station 6E). This location picks up frequencies from vortices being shed from the backward-facing step of the injector faceplate region. Of course, by the time shed vortices reach x-station 6E, some merging has already taken place and, consequently, the frequencies have been reduced in magnitude. Nevertheless, knowing the dominant frequency is important since the combustion zone is strong at this location. For all of the preceding cases, the dominant frequency ranges between 1.4 and 2.9 kHz at this location.

X. Conclusions

Axisymmetric unsteady Reynolds-averaged Navier–Stokes studies have been conducted to assess the hydrodynamic self-pulsations (unforced response) of the classical shear coaxial injector element used in many liquid rocket engines. Violent mass flow pulsations are created by the tremendous dynamic pressures imposed from the annular gas on the central liquid flow. Mechanisms for these pulsations include LOX post tip vortex shedding, acoustic pulsations within the LOX post, and injector faceplate region vortex formation. Vortical structures shed from the post tip interact in highly complex fashions in the recess region and tend to merge into larger structures as the flow emanates into the combustion chamber. As a result of these interactions, highly complex PSDs result when mass flow or field variable signals are processed. Post shedding and LOX tube acoustic modes can sometimes be fairly close to each other in practical designs; this factor further complicates the analysis of the data. As there is a substantial merging of vortices within the recess region, the faceplate shedding frequency is also challenging to ascertain under the demanding conditions typical of coaxial injector flows. The baseline case was operated at an O/F ratio of 10.3 and a F/O momentum ratio of 2.3. The dominant frequency across the entire injector recess region was equal to 7.6 kHz, which closely resembles the LOX post acoustic frequency. Low frequencies in the range of 2.2–2.7 kHz were observed inside the chamber, presumably due to vortex shedding from the backward-facing step of the injector faceplate region. By maintaining a constant hydrogen manifold pressure and varying the LOX manifold pressure, the O/F ratio was varied between 3.4 and 19.6.

Decreasing the O/F ratio leads to an accompanying decrease in dominant frequency at the injector exit plane, revealing that LOX velocity is dominating the flow. In addition, decreasing the O/F ratio (increasing F/O momentum ratio) leads to more diverse vortical structures, which create PSD plots of increasing complexity with multiple high-power frequencies. Because of larger shearing forces between the two fluid streams, increasing the F/O momentum ratio correspondingly leads to larger mass flow pulsations across the recess region. These flow pulsations are constant and low amplitude inside the LOX post and begin growing as the two fluid streams begin mixing at the LOX post tip plane. The flow pulsations reach a maximum shortly after the injector exit plane, and they begin a downward-sloping trend as the fluid expands into the chamber domain. The LOX post acoustic frequency is also one of the strongest frequencies inside the recess region for varying O/F ratios. Similar trends in mass flow pulsations and dominant frequency were observed when conducting variations in F/O momentum ratio by keeping the LOX manifold pressure constant and varying the gaseous hydrogen manifold pressure.

Variations in the LOX post thickness were performed by keeping the constant inflow pressures and cross-sectional areas. There was no strong variation in mass flow pulsations between the various thicknesses due to competing effects. The thick LOX post creates larger vortices, which consequently shed at lower frequencies. These lower shedding frequencies tend to dominate the LOX post acoustic pulsation in this case. In contrast, the thin LOX post creates smaller, higher frequency vortices that are not sufficiently strong enough to overcome the LOX post acoustic mode. For the thin-post case, the natural LOX post frequency dominates the frequency spectrum up to and slightly past the injector exit plane.

To investigate the effects of LOX post acoustic frequency, the length of the LOX post was decreased while maintaining all other variables constant. This led to a higher LOX post acoustic frequency, which created higher dominant frequencies inside the injector recess region. A similar behavior was observed when the LOX sound speed was varied by changing the LOX equation of state. The dominant pulsation frequencies are typically characterized by Strouhal numbers (based on LOX post thickness and LOX velocity) between 0.1 and 0.3.

While the study confirms prior assertions that post shedding, faceplate shedding, and LOX post acoustic modes are important, the interactions with other unsteady upstream structures (such as vena contracta instabilities) are still largely unknown. This is an area where future work would be desirable.

Acknowledgments

The authors wish to acknowledge the support of NASA under the Constellation University Institutes Program, managed by Claudia Meyer and Jeff Rybak. The authors would also like to thank Jeff West from the NASA Marshall Space Flight Center for his tremendous help with the Loci/CHEM code.

References

[1] Canino, J., Tsohas J., and Heister, S., "Dynamic Response of Coaxial Rocket Injectors," 42nd AIAA/ASME/SAE/ASEE Joint Propulsion Conference and Exhibit, Sacramento, CA, AIAA Paper 2006-4707, July 2006.

[2] Kim, B. D., and Heister, S. D., "Two-Phase Modeling of Hydrodynamics Instabilities in Coaxial Injectors," *Journal of Propulsion and Power*, Vol. 20, No. 3, 2004, pp. 468–479. doi:10.2514/1.10378

[3] Kim, B. D., and Heister, S. D., "Effect of Chamber Pressure Variation on High-Frequency Hydrodynamic Instability of Shear Coaxial Injector," 40th AIAA/ASME/SAE/ASEE Joint Propulsion Conference and Exhibit, Fort Lauderdale, FL, AIAA Paper 2004-3522, July 2004.

[4] Mayer, W., and Tamura, H., "Propellant Injection in a Liquid Oxygen/Gaseous Hydrogen Rocket Engine," *Journal of Propulsion and Power*, Vol. 12, No. 6, 1996, pp. 1137–1147. doi:10.2514/3.24154

[5] Oefelein, J., "Large Eddy Simulation of a Shear-Coaxial LOX–H2 Jet at Supercritical Pressure," 38th AIAA/ASME/SAE/ASEE Joint Propulsion Conference and Exhibit, Indianapolis, IN, AIAA Paper 2002-4030, July 2002.

[6] Lux, J., and Haidn, O., "Effect of Recess in High-Pressure Liquid Oxygen/Methane Coaxial Injection and Combustion," *Journal of Propulsion and Power*, Vol. 25, No. 1, 2009, pp. 24-32.
doi:10.2514/1.37308

[7] Jensen, R., Dodson, H., and Claflin, S., "LOX / Hydrocarbon Combustion Instability Investigation," NASA CR 182249, July 1989.

[8] Bazarov, V., Yang, V., and Puri, P., "Design and Dynamics of Jet and Swirl Injectors," *Liquid Rocket Thrust Chambers: Aspects of Modeling, Analysis, and Design*, edited by V. Yang, Vol. 200, Progress in Aeronautics and Astronautics, AIAA, Reston, VA, 2004., pp. 19–103.

[9] Bazarov, V., "Self-Pulsation in Coaxial Injectors with Central Swirl Liquid Stage," 31st AIAA/ASME/SAE/ASEE Joint Propulsion Conference and Exhibit, San Diego, CA, AIAA Paper 1995-2358, July 1995.

[10] Luke, E., "A Rule-Based Specification System for Computational Fluid Dynamics," Ph.D. Dissertation, Mississippi State Univ., Starkville, MS, 1999.

[11] Luke, E., Tong, X.-L., and Cinnella, P., "Numerical Simulations of Fluids with a General Equation of State," AIAA Paper 2006-1295, Jan. 2006.

[12] Luke, E., Tong, X.-L., Wu, J., Cinnella, P., and Chamberlain, R., "CHEM 3.2: A Finite-Rate Viscous Chemistry Solver: The User Guide," Mississippi State Univ., Starkville, MS, Oct. 2009.

[13] Cinnella, P., Luke, E., and Tong, X.-L., "A Thermodynamic Model for Chemically Reacting, Two-Phase Fluids," AIAA Paper 2006-1291, Jan. 2006.

[14] Gupta, R., Yos, J., Thompson, R., and Lee, K., "A Review of Reaction Rates and Thermodynamic and Transport Properties for an 11-Species Air Model for Chemical and Thermal Nonequilibrium Calculation to 30,000 K," NASA Rept. RP-1232, Aug. 1990.

[15] Menter, F., "Two-Equation Eddy-Viscosity Turbulence Models for Engineering Applications," *AIAA Journal*, Vol. 32, No. 8, 1994, pp. 1598–1605.
doi:10.2514/3.12149

[16] Venkatakrishnan, V., "On the Accuracy of Limiters and Convergence to Steady State Solutions," AIAA Paper 1993-0880, 1993.

[17] Roshko, A., "On the Development of Turbulent Wakes from Vortex Streets," NACA Rept. 1191, 1954.

[18] Tsohas, J., "Hydrodynamics of Shear Coaxial Liquid Rocket Injectors," Ph.D. Dissertation, Purdue Univ., West Lafayette, IN, 2009.

[19] Eisenlohr, H., and Eckelmann, H., "Observations in the Laminar Wake of a Thin Flat Plate with a Blunt Trailing Edge," *Experimental Heat Transfer, Fluid Mechanics, and Thermodynamics*, edited by R. K. Shau, E. N. Ganic, and K. T. Yang, Elsevier, New York, 1988, pp. 264–268.

[20] Droppers, L., Schuff, R., and Anderson, W., "Study of Heat Transfer in a Gaseous Hydrogen Liquid Oxygen Multi-Element Combustor," 43rd AIAA/ASME/SAE/ASEE Joint Propulsion Conference and Exhibit, Cincinnati, OH, AIAA Paper 2007-5550, July 2007.

[21] Hirschfelder, J., Buehler, R., McGee, H., and Sutton, J., "Generalized Equation of State for Gases and Liquids," *Industrial and Engineering Chemistry*, Vol. 50, No. 3, Part 1, 1958, pp. 375–390.
doi:10.1021/ie50579a039

[22] Tsohas, J., Canino, J., and Heister, S., "Computational Modeling of Rocket Injector Internal Flows," 43rd AIAA/ASME/SAE/ASEE Joint Propulsion Conference and Exhibit, Cincinnati, OH, AIAA Paper 2007-5571, July 2007.

[23] Canino, J., Heister, S., and Garrison, L., "Hydrodynamic Modeling of Oxidizer-Rich Staged Combustion Injector Flow," *42nd JANNAF Combustion Subcommittee Meeting*, Las Vegas, NV, 2004.

[24] Canino, J., Heister, S., Sankaran, V., and Zakharov, S., "Unsteady Response of Recessed-Post Coaxial Injectors," 41st AIAA/ASME/SAE/ASEE Joint Propulsion Conference and Exhibit, Tucson, AZ, AIAA Paper 2005-4297, July 2005.

A. Gupta
Associate Editor